Tampere University

Md Ajwaad Zaman Quashef

MODELLING AND CHARACTERIZATION OF HYBRID INTEGRATED LASERS IN 2 TO 3 µm WAVELENGTH BAND

Abstract

Md Ajwaad Zaman Quashef: Modelling and characterization of hybrid integrated
lasers in 2 to 3 µm wavelength band
Master's Thesis
Tampere University
Master's Degree Programme in Photonics Technologies
September 2023

Hybrid integrated silicon photonic lasers functioning at mid-IR wavelengths have
recently emerged as a solution for developing compact optical sensors targeted at
trace gas spectroscopy. This thesis concerns a measurement and simulation com-
bined approach to characterize Silicon Nitride photonic integrated circuits (PICs)
equipped to work as such lasers. Seven PICs from the same process are first aligned
in an end-fire coupling scheme with the III-V gain chip using a closed-loop piezo
stage. The gain chip consists of an AlGaInAsSb/GaSb type-I quantum well reflective
semiconductor optical amplifier (RSOA). The PICs contain narrow-band long rect-
angular spiral and round spiral shaped distributed Bragg reflectors (DBRs) which
work as external cavities allowing periodic feedback to the gain element. Intensity
vs. current sweeps and measurements of the spectra of the uncooled $\approx$2 μm lasers
demonstrate narrow full-width half-maximum (FWHM) linewidths and remarkable
power outputs in continuous wave operation at room temperature. The measure-
ments also give insight into process variation and design reliability, and have led to
a recent submission to Optica for publication. A commercial eigenmode expansion
solver is used to verify the experimental results as well as to explore the design space
for Bragg reflectors at 2 μm and 2.7 μm with a view to optimizing the packing ratio,
linewidth and side-mode suppression ratio of the devices for improved laser perfor-
mance. The rapid and efficient end-fire based optical testing method presented in
this work is expected to set a base-line for optimization of mid-IR tunable hybrid
lasers.

Keywords: GaSb, hybrid lasers, RSOA, silicon nitride photonics, mid-IR spec-
troscopy, Bragg grating, DBR, Eigen-mode expansion

The originality of this thesis has been checked using the Turnitin Originality Check
service.

Preface

This Master's thesis has been carried out at the Optoelectronics Research Centre (ORC), Tampere University (TUNI) with financial support from Business Finland project PICAP (44761). I would like to thank Dr. Jukka Viheriälä and Dr. Nouman Zia for acting as examiners for my thesis, and for their valuable advice and instructions which helped this work bear fruit in a short six-month span. I am grateful for the valuable mentoring and directions of Samu-Pekka Ojanen in the measurement and simulations, whose intuitive understanding of silicon photonics is very admirable. I also wish to thank An Nguyen for initially tutoring me in the Measurement lab, where the lion's share of my research was carried out.

I am grateful to the Erasmus+ programme for the Europhotonics Scholarship of which I am a beneficiary and whose mobility path led me to conclude my Master's education in Tampere. I would like to specially thank Tea Vellamo, the Europhotonics coordinator at TUNI, for her thorough directions and kind advice especially when first settling in Finland.

I am greatly indebted to my wife, whom I amazingly met during my Master's studies, for her care, emotional and mental support throughout my journey. And to my parents who are my constant source of motivation and inspiration though we are thousands of miles apart. Alhamdulillah, all praise is for God.

Tampere, 1 September 2023

Ajwaad

Contents

List of Figures

List of Abbreviations and Symbols

ARC	Anti-reflection coating
ASE	Amplified spontaneous emission
CMOS	Complementary metal–oxide–semiconductor
DBR	Distributed Bragg reflector
EME	Eigen-mode expansion
FP	Fabry-Perot
FWHM	Full-width-half-maximum
FTIR	Fourier-transform infrared spectrometer
GaSb	Gallium antimonide
HRC	High reflection coating
LI	Light (L)-Current (I)
MMF	Multi-mode fiber
MPW	Multi-project wafer
PIC	Photonic integrated circuit
RSOA	Reflective semiconductor optical amplifier
RT	Room temperature
SBGW	Spiral Bragg grating waveguide
Si_3N_4	Silicon Nitride
SMSR	Side mode suppression ratio
SNOI	Silicon nitride-on-insulator
SOI	Silicon-on-insulator
TE	Transverse electric
III-V	Element groups III and V

1 Introduction

The growing demand for photonic integrated circuits (PIC) in emerging system-on-chip applications is being propelled by the need to operate across an extensive optical bandwidth range, spanning from visible wavelengths (approximately 400 nm) to wavelengths exceeding the infrared threshold (greater than 2.3 μm). PICs are now capable of delivering performance levels that were once attainable only through bulk optic technologies. Driven chiefly by the large telecom and datacom market, the bulk of research on integrated photonics in the past two decades has focused on devices operating within the near-infrared (NIR) telecommunication bands near 1310 nm and 1550 nm wavelengths [1], [2]. This has been enabled primarily by leveraging the compatibility of the silicon (Si) photonic platform with existing complementary metal-oxide-semiconductor (CMOS) infrastructure for large scale electronics. Looking forward, the extension of the Si photonic platform to the the mid-infrared (MIR) spectrum (defined from 2 μm to 20 μm) will be a crucial advancement as it is a technologically important wave-band primarily for gas sensing [3], defense [4], and medical applications [5] (Figure 1.1). This is attributed mainly to the fact that numerous gases (such as H2S, C2H4, CH4, CO, CO2, N2O, and H2O) and biomolecules (like blood glucose, urea, and lactate [6]) exhibit pronounced absorption lines within this specific wavelength range. With a view to replacing bulky and power hungry conventional MIR spectroscopic systems, the emergence of photonic integration presents a promising avenue for creating cost-effective, energy-efficient, and compact sensors, as long as one can effectively integrate efficient and precisely tunable laser sources with a wide variety of PICs.
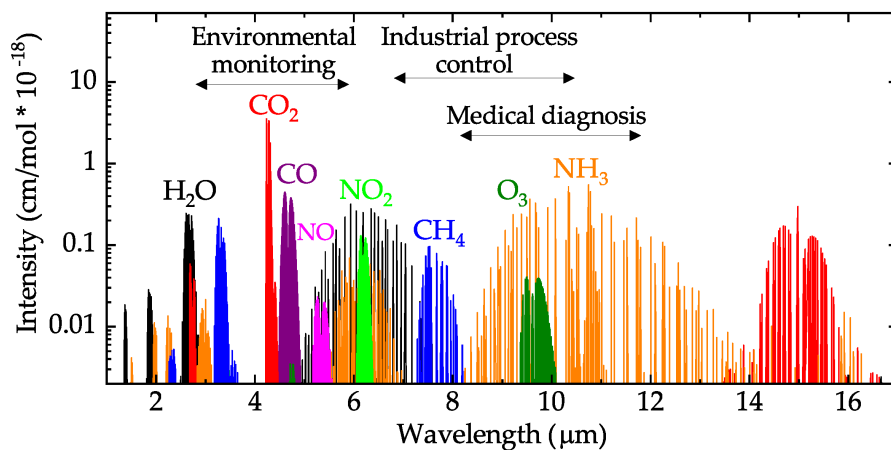
Figure 1.1 *Mid-infrared absorption spectra of gases and applicability. Adapted from [7].*

Because of the direct and tunable bandgap in addition to the high optical gain

of III-V semiconductors like InP, GaAs, InGaAs, GaSb etc., there has been intense research in the area of III-V-on-silicon integration [8], [9] for on-chip light sources. When it comes to achieving MIR emission between $2 - 3$ μm, GaSb is an attractive platform exhibiting high gain thresholds and low operation voltages. GaSb-based type-I quantum well (QW) reflective semiconductor optical amplifiers (RSOA) have excelled in performance exhibiting emission up to 3.7 μm [10], [11]. Continuous wave mode operation of GaSb tunable lasers hybridly integrated on Silicon-on-insulator (SOI) and Si_3N_4 have recently been demonstrated near 2 μm [12], [13] and 2.6 μm [14]. Whatever be the application, the appropriate III-V heterostructures used to build active components like lasers, amplifiers and modulators are integrated on passive PICs through direct epitaxial growth, heterogeneous, and hybrid approaches. Among these, epitaxial growth is a monolithic integration solution and has been demonstrated primarily for the O-band (around 1310 nm) [15]. Heterogeneous integration is a rapidly maturing approach developed to combine III–V materials with silicon photonic waveguides [16], [17]. One of the disadvantages of this approach is that it does not allow for component-wise modular testing before integration into more complex PICs [15]. Hybrid integration is the most straight-forward and mature approach allowing integration of PICs available from foundries as well as separate optimization and thermal management of active and passive chips [18]. It is especially convenient for the testing stage of PIC components as it enables one to choose the best performing devices and discard non-functional ones. Butt-coupling is a flexible hybrid integration method based on critical mode-matching of active and passive chips at the interface and has been used to demonstrate narrow linewidth single mode and mode-locked lasers using a Si_3N_4 feedback circuit and an InP active chip [19], [20], as well as the mentioned GaSb tunable lasers.

Presently, silicon-on-insulator (SOI) technology stands as a prominent choice for achieving high-volume photonic integration using the conventional CMOS infrastructure. In traditional SOI photonics, waveguides with a significant index contrast are fabricated, featuring a silicon core surrounded by SiO_2 insulator cladding. This design leads to robust mode confinement and facilitates the creation of compact circuits that can handle tighter bends. Another well-established foundry-scale process employs group III–V photonics materials, such as indium phosphide (InP). InP offers waveguides with optical gain and efficient signal modulation, particularly in the telecommunications wavebands. Complementing both the SOI and III–V photonics platforms, silicon nitride (Si_3N_4) waveguide technology has emerged as a CMOS-compatible alternative, introducing a new generation of system-on-chip applications that may not be attainable with the other platforms on their own. In contrast to the SOI and InP platforms, Si_3N_4 waveguides cladded by SiO_2 (silicon nitride-on-insulator, SNOI) have relatively low index contrast, making them less

prone to waveguide scattering and thus able to offer ultra-low propagation losses [21]. Consequently, these waveguides can offer orders-of-magnitude longer optical cavities compared to III–V-based waveguides, greatly enhancing laser linewidth capabilities to sub-kHz and Hz-levels [19], [22], [23]. Si_3N_4 has gained recognition for its minimal nonlinear absorption characteristics and extensive transparency range, enabling broadband operation from the visible spectrum to wavelengths exceeding 2 μm. Consequently, it has emerged as an appealing choice for multi-spectral sensing applications. The commercialization of Si_3N_4-based photonic integrated circuits (PICs) and their associated chip design tools has reached a mature stage, involving collaborations with external foundries and Multi Project Wafer (MPW) production runs [24].

Upon making an appropriate choice of gain material and passive platform, wavelength selectivity in the $2 - 3$ μm range is enabled in principle by tunable lasers. In sensing applications, the capability to access numerous absorption features is frequently essential for identifying different trace substances. Greater sensitivity and selectivity in measurements is vital and can be accomplished by employing a widely tunable narrow-linewidth laser, allowing for tuning to multiple wavelengths within the SOA's gain bandwidth. External cavity lasers (ECL) can provide much wider tuning and narrower linewidth compared with vertical cavity surface emitting lasers (VCSEL) and distributed feedback (DFB) lasers [12]. Traditional ECLs (e.g. based on the Littrow configuration) require a bulky optics system and mechanical controllers [25]. Alternatively, silicon or Si_3N_4 external cavity structures implemented through hybrid III-V/PIC technology can significantly shrink the overall physical size. Among ECLs, the requirement of a combination of narrow linewidths, tunability, and low power consumption has raised a greater interest in single-mode DBR and DFB lasers. DBR lasers are inherently more power efficient as the optical losses within the laser cavity and the electrical resistances are inherently lower [26]. While a Bragg grating by itself is more suitable for fine tuning (<10 nm[27]), hybrid DBR cavity laser cavities incorporated with thermally tunable Mach-Zehnder interferometers [28] and microring resonators [29] have recently been demonstrated with >70 nm tuning range in the 2-3 μm window.

This work seeks to set a base-line for optimization of mid-IR tunable hybrid lasers operating in the 2-3 μm wavelength range, by implementing a measurement and simulation combined approach to characterize SNOI PICs equipped with long spiral shaped DBRs. By achieving low coupling loss end-fire alignment of an AlGaInAsSb/GaSb type-I quantum well (QW) RSOAs gain chip with multiple SNOI PICs, we build single mode hybrid lasers and characterize their lasing performance (peak power, lasing threshold, linewidth, side-mode suppression etc.) in a home-built optical setup. This allows us to study the design parameters of the RSOA

and the external cavity individually, as well as the coupling mechanism, in order to optimize the laser performance specifically for application in mid-IR spectroscopy.

1.1 Objectives

The main research objectives of this thesis are as follows:

- Reliably achieve low-loss optical alignment of III-V gain chip with SNOI PICs to form hybrid laser cavities over a set of repeated measurements.

- Model narrow-band first-order gratings to optimize the packing ratio, reflectance profile and side-mode suppression ratio without sacrificing single-mode operation in 2 to 3 μm wavelength band.

- Characterize light-current (peak power, lasing threshold, thermal rollover) and spectral performance (linewidth, side-mode suppression, center wavelengths) of rectangular spiral and round spiral DBR external cavity lasers at 2 μm under continuous-wave operation.

- Evaluate process variation and design reliability of laser PICs from same wafer process.

1.2 Thesis Organization

This thesis is organized into five chapters.

Chapter 1 briefly lays out the development and advantages of silicon photonics especially in the mid-IR range and presents the motivation and objectives of this thesis.

Chapter 2 provides relevant literature review and discussion on the integrated photonic platforms, especially the silicon nitride platform. Available III-V sources on PICs and integration methods for the sources on this platform are discussed. Finally, principles of silicon Bragg grating waveguides and spirals as external cavities for integrated lasers are reviewed.

Chapter 3 presents the design of the round spiral and rectangular spiral grating waveguide on the SNOI PIC. A number of design variations for these waveguides are theoretically analyzed and simulated at two different wavelengths. design.

Chapter 4 begins with a discussion regarding how the gain chip was characterized and a description of the alignment and measurement system used to characterize the lasers. The experimental results of laser performance and variation are analyzed and compared with the numerical simulations.

Chapter 5 presents the summary and conclusions for the work as well as some suggestions for future improvements of the measured Si_3N_4 DBR lasers.

2 Theoretical Background

This chapter is intended to provide a brief overview of the current state of silicon nitride photonics and light sources available on the platform, especially those based on GaSb technology. Discussions on the hybrid method of integrating lasers on the platform and its applications are provided. The chapter concludes with an overview of the principles and design methods of integrated Bragg gratings with relevance to hybrid lasers.

2.1 Integrated Photonic Platforms

A photonic integrated circuit (PIC) combines multiple optical elements on a single chip and typically consists of a substrate on which a low- and high-refractive index material layer are grown or deposited. Over the years PICs have been demonstrated in a wide range of material systems and platforms, each with their obvious advantages and shortcomings. The material platforms which are currently offering generic processes for realization of PICs are the InP platform [30], the silicon-on-insulator (SOI) platform [31], [32], and the Si_3N_4-on-insulator (SNOI) platform [33]–[35].

The extensively utilized group III–V photonics material, indium phosphide (InP), represents another foundry-scale process renowned for providing waveguides with optical gain and efficient signal modulation within the telecommunications wavebands [33]. InP finds applications both as a standalone photonic integrated circuit (PIC) and as a gain block for SOI PICs. However, this comes with a trade-off in terms of higher waveguide losses, ranging from 2 to 0.4 dB/cm [36], and the necessity for larger bend radii. In the realm of mid-infrared (mid-IR) photonics, intrinsic $In_{0.53}Ga_{0.47}As$ and InP materials exhibit near-complete transparency across the entire molecular fingerprint region (from $\lambda = 3$ to 15 μm). Furthermore, $In_{0.53}Ga_{0.47}As$/InP waveguides offer a well-established lattice-matched platform characterized by very low defect density. This makes them suitable for constructing integrated optical circuits with minimal optical losses [37].Though it is the only mainstream platform offering monolithic integration of light sources (e.g. quantum cascade lasers), overcoming performance deteriorations above 2 μm and high cost of fabrication is still an objective of active research [38].

As one of the most promising integrated optics platforms, SOI was initially developed for ultrahigh-speed data transmission in computing systems and data centers. SOI leverages the complementary metal–oxide–semiconductor (CMOS) infrastructure from the large scale micro-electronics industry. In traditional SOI photonics, waveguides with high contrast are utilized. These waveguides consist of a silicon

core enveloped by an oxide (SiO₂) cladding, effectively confining the light within the core. This robust confinement mechanism results in the creation of highly compact photonic circuits characterized by small bend radii and moderate waveguide losses, typically in the range of approximately 0.1 dB/cm [2]. Si has the drawback of low bandgap (corresponding to the wavelength of ∼1 μm), which ultimately limits the operational wavelengths to the infrared. On the other side of the spectrum, two-photon absorption in the wavelength range between 1.55 and 2 μm [39] strongly increases waveguide losses for high-power applications and limits the usage of the SOI platform. When operating at wavelengths exceeding 2.5 μm, the oxide cladding in silicon waveguides starts to exhibit losses, as reported in [40]. In mid-infrared (mid-IR) silicon waveguides, the primary source of loss arises from the absorption of the mode that partially overlaps with the cladding surrounding the waveguide core on all sides. The extent of this mode overlap with the cladding, especially in the case of high-index contrast waveguides, can be adjusted by modifying the cross-sectional geometry or, more commonly, by altering the thickness, as depicted in Figure 2.1. The utilization of silicon-on-insulator (SOI) waveguides with thicknesses in the micrometer range (μm) is more advantageous beyond 2 μm wavelengths compared to the conventional sub-micron SOI waveguides. This is due to their ability to strongly confine the mode, resulting in lower transmission losses [41].
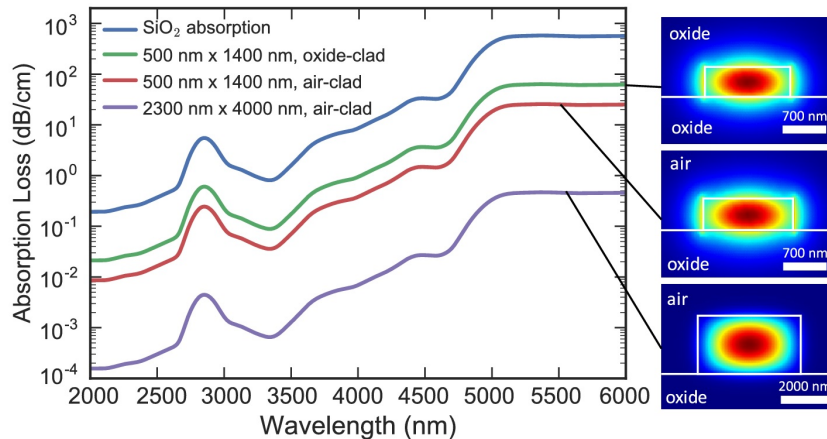
Figure 2.1 *Simulated absorption losses vs. mid-IR wavelengths for different waveguide thickness, including a traditional silicon photonic waveguide for this wavelength with 500 nm thickness (green) as well and a thicker 2300 nm waveguide (blue). Removing the top cladding (red) shows a modest improvement in loss, limited still by the large remaining overlap with the under-cladding. The cladding oxide absorption is plotted in the blue curve. Inset shows the FEM simulations of mode profiles. Adapted from [41].*
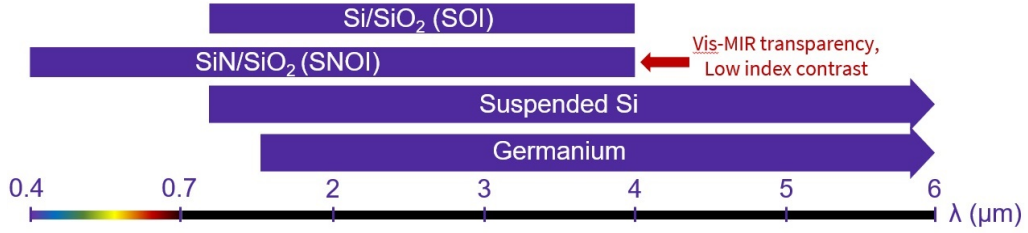
Figure 2.2 *Window of transparency (white colored) for different material systems used in photonic integration*

2.1.1 Silicon Nitride Photonic Platform

Silicon nitride (Si_3N_4) PIC technology provides lower loss waveguides and building blocks complimentary to SOI and InP PICs, and are also compatible with CMOS processing. As shown in Figure 2.2, Si_3N_4 has a wider transparency window (i.e., from the visible to the near-infrared, 400 nm to 4 μm). This has led to applications across a broad spectrum- in microwave photonics, the Si_3N_4 waveguides are used for beamforming systems [42] and programmable signal processing chips [43]. In non-linear optics, optical combs [44], [45] and supercontinuum generation [46], [47] are demonstrated using thick Si_3N_4 waveguides with high mode confinement. In the bio-sensing field, interferometric sensors [48], fluorescence imaging [49] and Raman spectroscopy [50] on the Si_3N_4 platform have been demonstrated. More recently, the Si_3N_4 platform are presented in range and position sensors for autonomous drive technologies such as LIDAR [51] and optical gyroscopes [52].

In search of technologically advanced alternatives to SOI, Si_3N_4 emerges as a viable option [53]. In fact, it proves to be a better passive CMOS-compatible material in many directions compared with Si owing to its various advantages, such as a moderate refractive index, lower sidewall roughness, scattering loss with very high tolerance to dimension variations, and absence of two-photon absorption. At mid-IR wavelengths, Si_3N_4 waveguides exhibit low propagation losses successfully growing thicknesses up to 950 nm [34], while 800 nm Si_3N_4 technology is available through the LIGENTEC foundry open-access MPW run [54]. The MPWs are built on a cost-sharing model so as to allow easy and low-cost access to standardized processes for rapid and proof-of-concept prototyping. Companies such as Lionix [55] and IMB-CNM [56] are other established commercial providers.

While state-of-the-art silicon modulators rely on phase modulation through free carrier plasma dispersion in p–n, p–i–n, and MOS junctions, these solutions are not viable using Si_3N_4 due to its insulating nature. Nonetheless, electro-optic modulators on SNOI based on the nanophotonic Pockel's effect using PZT [57] and

graphene [58] have achieved modulation bandwidths over 30 GHz. Heaters utilising the thermo-optic (TO) effect are viable for wavelength or phase tuning, but comparatively power-inefficient since the thermo-optic coefficients of Si_3N_4 and SiO_2 are an order of magnitude smaller than Si. However, this also means that a Si_3N_4 waveguide will be far less sensitive to temperature variations than one based on Si or InP. Enhancing thermal performance can be achieved by employing a thicker Si_3N_4 waveguide, which in turn increases the optical confinement factor, effectively preventing mode leakage into the SiO_2 layer, which possesses an even lower TO coefficient [18].

2.2   III-V Gain Chip Technology

A significant challenge in silicon photonics platforms is the absence of an on-chip light source. The integration of fully self-contained lasers becomes crucial as it eliminates the necessity for free-space or optical fiber coupling to waveguides, leading to improvements in both device scalability and stability. Silicon, due to its indirect bandgap, does not support efficient light generation, let alone laser operation [59]. Consequently, over the past two decades, there has been a substantial surge in research and development efforts aimed at integrating light sources directly onto silicon photonic chips [9], [60]. Because of the direct bandgap and the high optical gain of III-V semiconductors, it has been the norm to integrate III-V lasers via heterogeneous and hybrid integration methods, which are discussed in the next section. Suitable active materials that can be used to provide gain at telecommunication wavelengths are generally based on InP ternary and quaternary epitaxial layer stacks with InGaAsP or InGaAlAs [61]–[63]. For applications requiring wavelengths in the range 650–1100 nm, GaAs based VCSELs with high modulation bandwidths [64] are an attractive source for integration on a silicon nitride waveguide platform.

In terms of mid-IR light sources, QCLs and ICLs cover almost the entire mid-IR spectrum (3–20 μm) and are now available as commercial off-the-shelf (COTS) components [65], [66]. However, at the shorter wavelength end of the spectrum where room temperature operation of cascade lasers is yet to be realized, classical diode lasers based on type-I or type-II semiconductor heterostructures offer the best performance so far. InP-based type-I heterostructures can reach upto 2.3 μm with highly strained epitaxial conditions, while extension to 2.7 μm has been reported, but laser operations occur below room temperature [67], [68]. These are also quite temperature sensitive as they have large thermo-optic coefficients (dn/dT). When it comes to CW operation at or beyond room temperature, GaInAlAsSb/GaSb-based type-I laser diodes have demonstrated exceptional performance within the 2–3 μm wavelength range. They excel by providing substantial gain with relatively low threshold currents and operating at a low voltage. [69], [70]. Hybrid GaSb/SOI and

GaSb/SNOI lasers in the 2-2.6 μm range have been reported [12], [71], and by this research group [14] demonstrating record wavelength tunability ($>$ 170 nm) [72].

The gain chips used in this work were GaSb based reflective semiconductor optical amplifiers (RSOA), whose waveguide structure is similar to that of a superluminescent diode (SLD) but utilize a high reflectivity coating on one side to be able to form one end of a laser cavity. The working principle of an RSOA or SLD is based on amplified spontaneous emission (ASE) whose broadband nature is similar to a light emitting diode (LED) while the beam quality is similar to a laser diode (LD). [73]. RSOAs are easy to collimate, focus, and couple into an optical fiber or a silicon waveguide. Figure 2.3 shows the heterostructure for SLDs grown via molecular beam epitaxy (MBE) for this work designed to work at 2 μm.

2000 nm SLD

200 nm p-GaSb cap
n = 1.10^{19} cm^{-3}

1500 nm p-Al$_{0.5}$Ga$_{0.5}$AsSb cladding, n = 1.10^{18} cm^{-3}

500 nm p-Al$_{0.5}$Ga$_{0.5}$AsSb cladding, n = 2.10^{17} cm^{-3}

500 nm n-Al$_{0.5}$Ga$_{0.5}$AsSb cladding, n = 2.10^{17} cm^{-3}

2000 nm n-Al$_{0.5}$Ga$_{0.5}$AsSb cladding, n = 1.10^{18} cm^{-3}

300 nm GaSb buffer

GaSb substrate

130 nm Al$_{0.3}$Ga$_{0.7}$AsSb waveguide

2x10 nm Ga$_{0.82}$In$_{0.22}$Sb Qws with 20 nm Al$_{0.3}$Ga$_{0.7}$AsSb barrier

130 nm Al$_{0.3}$Ga$_{0.7}$AsSb waveguide

***Figure 2.3** Schematic of the hetero-structure of 2 μm SLDs used for this work, showing the active region consisting of type-I double quantum wells embedded in a AlGaAsSb waveguide. Adapted from [74]*

More specifically, the RSOA utilized a type-I double quantum well structure with a length of 2000 μm to generate gain and facilitate cavity feedback within the laser circuit. It incorporated a single-mode ridge waveguide (RWG) with a width of 5 μm and featured a distinctive "J-shaped" configuration (as shown in Figure

2.4). In this layout, the RWG comprised a bent waveguide with a 7° output angle at the front facet. This J-shaped waveguide design served as an effective means to suppress unwanted laser oscillations within the RSOA cavity itself, as discussed in [75]. By doing so, it minimized optical feedback at the front facet, while the rear facet remained straight to provide reflection for a double-pass configuration. The advantage of this particular design lies in its ability to effectively double the effective gain length without changing the actual waveguide dimensions. As a result, the cumulative gain increase contributes to the output power of the gain chip. The curvature of the RWG bend adhered to an Euler spiral geometry, characterized by linearly increasing curvature along the bend, which helped reduce mode losses, as explained in [76]. The rear facet was left in its as-cleaved state and provided approximately 30% reflectance.
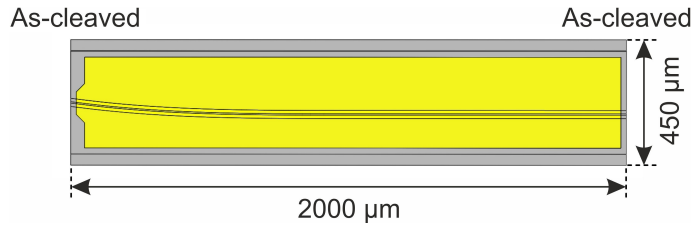
Figure 2.4 Schematic of the RSOA used in this work, showing the RWG bend at the front facet (left) for reflection suppression.

2.3 Hybrid Photonic Integration Methods

There are mainly three approaches to integrate III-V gain materials on PICs to build lasers. These are: epitaxial growth (aka monolithic integration), heterogeneous integration, and hybrid integration. Monolithic integration offers a method for directly growing III-V compound semiconductor materials on group IV substrates, utilizing techniques like molecular beam epitaxy (MBE), chemical vapor deposition (CVD), or vapor phase epitaxy (VPE). The primary challenge in this process stems from the substantial mismatch between the lattice constants and thermal expansion coefficients of silicon (Si) and III-V materials, leading to considerable power losses in devices [77]. To mitigate this issue, the use of intermediate buffer layers, typically made from materials like germanium (Ge) and strained superlattices, is necessary to minimize the propagation of dislocations into the active region. Recent findings have shown remarkable improvements in the lifetime of epitaxially grown quantum dot (QD) lasers on silicon, surpassing the performance of similar quantum well lasers [78].

Heterogeneous integration is a relatively mature technology to integrate III-V laser on a Si substrate via wafer bonding or flip-chip bonding techniques [79]. This

process is generally performed at the early to mid-stages of fabrication of the PIC chip, e.g. unpatterned III–V thin-films integrated onto pre-processed silicon photonic wafers. While heterogeneous approaches like transfer printing [80] have been lauded for high thoroughput of integrated lasers at NIR, it has not been fully extended into the 2-4 μm regime, with RT CW operating InP-based QW lasers at 2.0 μm [81] and sub-RT operation at 2.3 μm [29] having been the longest lasing wavelengths reported.
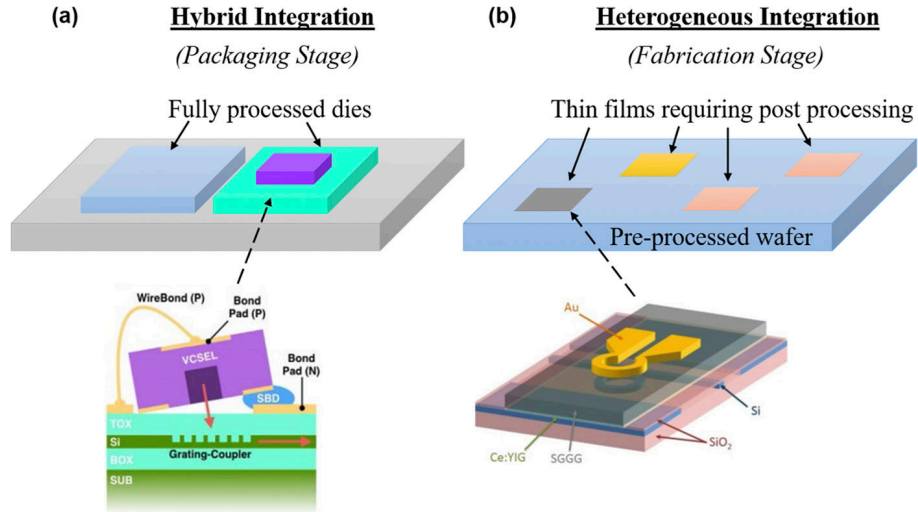
***Figure* 2.5** *Schematic illustration of (a) hybrid and (b) heterogeneous integration, with examples shown as insets. Adapted from [15].*

Hybrid integration represents one of the most straightforward and practical methods for combining processed photonic chips, typically sourced from different material technologies, into a single package. The key advantage of hybrid integration lies in the availability of commercially produced gain chips and the ability to independently fabricate and test high-performance devices on the passive platform. This approach enables the selection of the best-performing components while discarding non-functional ones, thereby increasing overall yield and facilitating tighter performance control. In a hybrid flip-chip approach, processed chips can be directly mounted on top of the photonic integrated circuit (PIC). This method has been successfully demonstrated on SOI for various devices, including VCSELs [82], InP-based RSOAs [83], RSOA arrays [84], and semiconductor mode-locked lasers (MLL) [85]. Another flexible method for chip-scale optical interconnection between processed chips is photonic wire bonding [86]. In the context of wavelengths around 2 μm, a significant milestone was achieved with the introduction of the first entirely on-chip GaSb/SOI hybrid laser [27]. This development involved integrating a GaSb RSOA with a micrometer-scale thick SOI-based Distributed Bragg Reflector (DBR) mirror using a flip-chip configuration through end-fire coupling. One of the most commonly

employed approaches in hybrid integration is the combination of commercially available standard III-V Semiconductor Optical Amplifiers (SOAs) with external SNOI or SOI cavities through facet bonding, often referred to as butt-coupling.

Butt coupling has its name from the coupling process, which requires the butting of the two devices to be interfaced in a way that enables the coupling of the mode field of the transmitter to the receiver device [87]. The coupling efficiency (which greatly impacts laser performance) depends on several factors [88]: (1) the quality of the end facets, (2) the angle of light reflection from the end facet, (3) the spatial alignment of the modes, and (4) the matching of the modes in the two material technology interfaces. The mismatch loss can be reduced to below 1 dB by carefully designing a box-like spot size converter (SSC) on the passive chip [89], [90] or designing inverse tapers on both the active and passive chips [91]. A disadvantage is that the photonic device alignment and integration process is a serial process (one device or one bar of devices at a time), which can be time consuming and have limited throughput.

2.3.1   Integrated External Cavity Lasers

Hybrid integration methods are popular for fabricating external cavity lasers (ECL) which offer narrow linewidths and high SMSR [92]. The EC architecture using separate gain and passive chips allows for the flexibility to optimize the grating mirror reflectance, bandwidth, and laser cavity length in the passive chip, and optimize the loss and efficiency in gain material, independently from each other. Figure 2.6 shows an example configuration. Various external cavity structures including Fabry-Perot (FP) cavities [93], distributed feedback (DFB) gratings [94], Bragg gratings [95], [96], sampled grating distributed Bragg reflectors (SG-DBR) [97], interferometric structures [98] and Vernier microring resonators (MRRs) [13] have been demonstrated. Previous studies have demonstrated that DBR based ECLs exhibit remarkably narrow linewidths at the kHz-level in the 1.55 μm wavelength range [96], thanks to long cavity lengths enabled by packing of long reflectors into spiral shapes on the PIC.
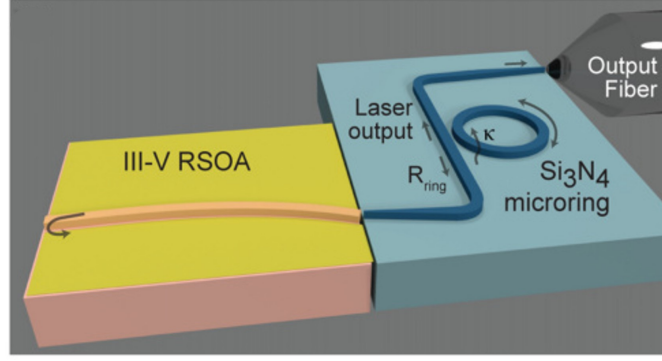
Figure 2.6 *Example schematic of an external cavity laser formed by butt-coupling of RSOA active chip and SNOI microring resonator from [99]*

2.4 Bragg Gratings

In the simplest configuration, a Bragg grating is a structure with periodic modulation of the effective refractive index (n_{eff}) in the propagation direction of the optical mode, as shown in Figure 2.7. This modulation is commonly achieved by varying the refractive index (e.g., alternating material) or the physical dimensions of the waveguide. At each boundary, a reflection of the travelling light occurs, and the relative phase of the reflected signal is determined by the grating period and the wavelength. The repeated modulation of the effective index results in multiple and distributed reflections. The reflected signals only interfere constructively in a narrow band around one particular wavelength, namely the Bragg wavelength [100] which is given as:

$$\lambda_0 = 2\Lambda_G n_{eff}(\lambda_0) \tag{2.1}$$

where Λ_G is the grating period and n_{eff} is the average effective index of the structure at the Bragg wavelength. Eqn. 2.1 predicts a red shift of the Bragg wavelength for a shorter modulation period and a blue shift for a longer period. A change of the average effective index, for example caused by a waveguide bend which perturbs the propagation mode, or by a stronger modulation (i.e. increasing n_{eff2}), would also shift the resonance peak of the grating.
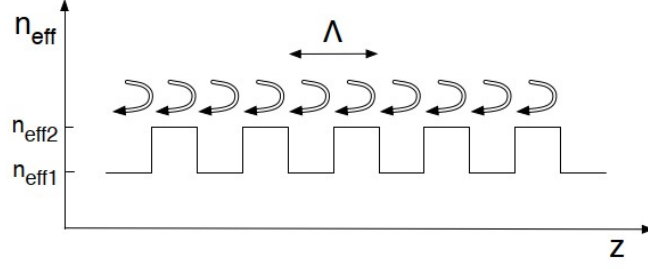
Figure   2.7 *Longitudinal effective index profile of a uniform grating [100].   z is the propagation direction, Λ is the grating period, n_{eff1} is the low effective refractive index and n_{eff2} is the high effective refractive index.*

The power reflectivity (alternatively referred to as reflectance) of a finite length uniform Bragg grating is given by:

$$R = \frac{|\kappa|^2 \sinh^2(sL)}{s^2 \cosh^2(sL) + (\Delta\beta/2)^2 \sinh^2(sL)} \tag{2.2}$$

where κ is the coupling coefficient, L is the grating length, and $\Delta\beta$ is the propagation constant deviation from the Bragg wavelength, which is related to the parameter s and κ through the expression:

$$s^2 = |\kappa|^2 - (\Delta\beta/2)^2 \tag{2.3}$$

For the case where $\Delta\beta = 0$, Eqn 2.2 gives the peak power reflectivity at the Bragg wavelength:

$$R_{peak} = \tanh^2(\kappa L) \tag{2.4}$$

In one grating period, the reflection at each interface can be expressed as: $\frac{n_{eff1}-n_{eff2}}{n_{eff1}+n_{eff2}}$. Since each grating period includes two interfaces, the coupling coefficient κ can be written as:

$$\kappa = 2\frac{n_{eff1} - n_{eff2}}{n_{eff1} + n_{eff2}}\frac{1}{\Lambda} = \frac{\Delta n}{n_{\text{eff}}\Lambda} = \frac{2n_{\text{eff}}\Delta n}{n_{\text{eff}}\lambda_0} = \frac{2\Delta n}{\lambda_0} \tag{2.5}$$

Eqn. 2.4 demonstrates that the grating reflectivity improves by increasing the total grating length or alternatively put, the number of periods. R_{peak} also improves by increasing the coupling strength κ, which from Eqn. 2.5 means that structures with larger index contrast are capable to reflect the Bragg wavelength more strongly. If the perturbations are weak however, which is the case for SNOI waveguides (in contrast to SOI), longer grating are required to get the same reflectance performance. Noticeably, κ does not depend on the value of the average effective index but on the difference between higher and lower index.

The bandwidth is another critical figure of merit for Bragg gratings. The reflection

bandwidth between the first nulls around the main reflection peak of a grating structure is defined as:

$$\Delta\lambda = \frac{\lambda_0^2}{\pi n_g}\sqrt{\kappa^2 + (\pi/L)^2} \qquad (2.6)$$

where n_g and L are the group index and total grating length respectively. Evidently, though the bandwidth can be unconditionally improved with a longer grating, for sufficiently long gratings ($\pi/L << \kappa$), the bandwidth is primarily determined by κ. Though it improves the reflectivity, stronger coupling in grating structures also widens the resonance peaks. Consequently, the lasers cavities result in broader linewidth of lasing. It is to be noted that this bandwidth is larger than the 3-dB bandwidth, which is also often used for the characterization of Bragg gratings. It should also be noted that, for the sake of simplicity, the analysis above assumes that the grating is lossless, but losses can be accounted for using an appropriate imaginary term in the propagation constant.

2.4.1 Silicon Photonic Bragg Gratings

Practically on an integrated photonic platform, A Bragg grating is a structure formed within a waveguide with physical corrugations that cause a modulation in the effective refractive index of the waveguide. These perturbations are typically very subtle, with a refractive index change (Δn) on the order of 10^{-3}. To achieve a high reflectivity in the grating, a considerable length is required, often in the range of tens of millimeters. However, from a layout perspective, such long gratings are often undesirable because their high aspect ratio makes efficient integration challenging. Additionally, longer Bragg gratings are more susceptible to variations in the thickness of the Si_3N_4 layer, which can impact their performance. Therefore, it becomes essential to pack long Bragg gratings into a smaller area. Spiral configurations have proven to be highly effective for compactly arranging lengthy waveguides, as discussed in [101]. In a spiral design, the straight-line distance between any two points on the grating is minimized, which, in turn, reduces the variations in waveguide thickness within the grating. Figure 2.8 illustrates a typical round spiral design where two semi-circular waveguides create an S-shaped configuration at the center of the device, with two interleaved Archimedean spirals connected to the S-shaped waveguide. Both semi-circular waveguides have the same radius of curvature, denoted as R_0. The spiral Bragg grating waveguide (SBGW) has two ports.
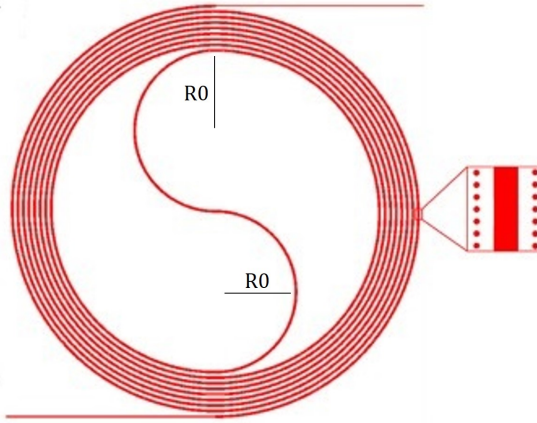
Figure 2.8 *Schematic of a Si_3N_4 SBGW. Inset shows the zoomed view of periodic modulations.*

3 Design and Simulations

In this chapter, the designs for the fabricated Bragg grating structures are described. Numerical simulations of the structures are presented with a view to verifying the experimental results and exploring the design space for Bragg reflectors.

3.1 Cladding Modulated Bragg Grating Design

To achieve a sufficiently narrow DBR reflectance band, a very weak change in index (following Equation 2.6) on the order of 10^{-3} is required. This is very difficult to achieve with a regular corrugated DBR, as it requires varying the width on the order of 5–10 nm, very close to the minimum resolution of the MPW process. Periodic index change was therefore achieved in an alternative design, by placing circular posts periodically next to the strip waveguide [102]. The grating strength of such structures can be controlled by varying the radii of the cylinders or the coupling gap. Due to the smaller overlap between the light mode and the index perturbation structures compared with conventional sidewall Bragg gratings, cladding-modulated gratings can easily achieve weak coupling and thus narrow-band spectra. A Lorentzian linewidth of 320 Hz at the C band for a Si_3N_4 post grating based laser was reported in [22].
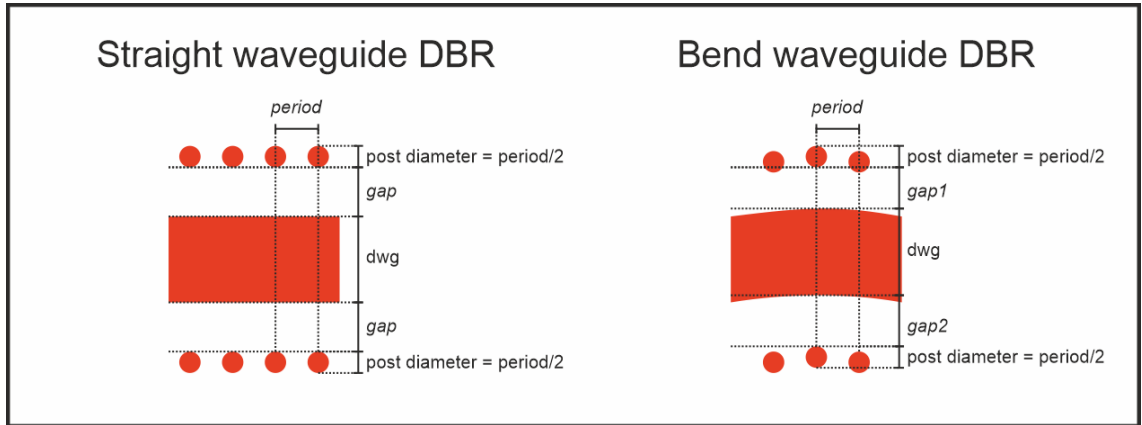
Figure 3.1 *DBR waveguide design and parameters*

We used the Ansys Lumerical Finite Difference Eigenmode (FDE) solver utilizing SiO_2 absorption values from literature [103] to simulate the mode profiles as shown in Figure 3.2(a). We noted that bending losses are negligible for the bending radii of fabricated round spirals (>145 μm) by comparing the fundamental transverse electric (TE) mode propagation loss with that in a straight waveguide. Figure 3.2(b) visualizes the control of the refractive index contrast and thus the grating strength

by (symmetrically) varying the gap between the grating posts and waveguide. Considering Eqn. 2.5, it is evident that that the grating coefficient or grating strength decreases with increasing gaps.
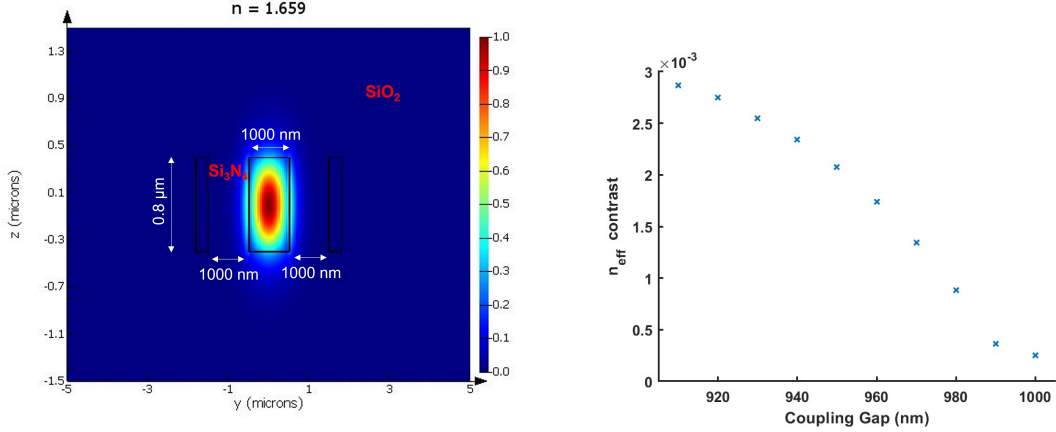
Figure 3.2 *(a) Electric field distributions of the fundamental TE mode in an SNOI waveguide with a 145 µm bend radius. The propagation loss is 0.065 dB/cm at 2 µm and 0.68 dB/cm at 2.7 µm; (b) Variation of effective index contrast (Δn) at 2 µm as a function of post coupling gap*

3.2 Si₃N₄ PIC Design

3.2 Si_3N_4 PIC Design

The cladding modulated grating was packed into round spiral and rectangular spiral shapes (on separate PICs) designed to provide reflection peaks near around 2 µm. For the round spiral DBRs, seven PICs with two 20 mm long spirals each, were fabricated using the same MPW run using LIGENTEC open-access foundry services [54]. They had a 225 µm long inverse taper at the input waveguide, tapering from a width of 0.4 µm to 1 µm to minimize mode mismatch at the working wavelength [27]. The inverse taper was tilted at an angle to match the output angle of the RSOA. Each PIC had two cavities (labelled H01 and H02), designed for a nominal resonance of 1994 nm and 2004 nm respectively. Figure 3.3 shows the grating structures consisting of two interleaved Archimedean spirals separable into 10 segments of incrementally varying bend radii. The bend radius for the 9 outer waveguide bends was set to 290 - 370 µm while the inner S-bend had a radius of 145 µm. The duty cycle of the grating was 50%, while the radius of the posts were set to approximately one-fourth of the period. The coupling gap on both sides of the Si_3N_4 waveguide was set to 1000 nm and was constant along the spiral. The spacing between two adjacent half circles, or the spiral pitch, is set sufficiently long to 9 µm to ensure low crosstalk coming from evanescent coupling between waveguides. We noted that this value is quite conservative and could be reduced (e.g. to 5 µm) to further improve

the packing efficiency.
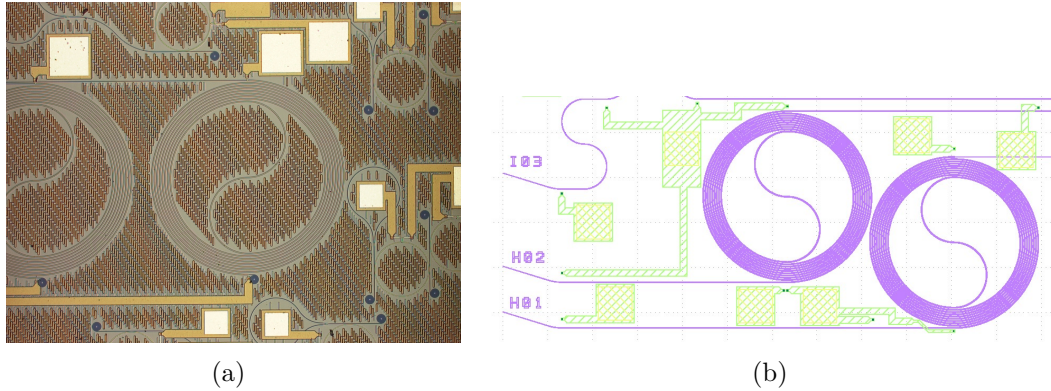
Figure **3.3** *(a) Microscope image and (b) mask layout of two 20 mm long SBGWs wrapped into an area of $\approx 0.43mm^2$ each*

One PIC contained two rectangular spiral DBRs designed for slightly different wavelengths (1992 nm and 2002 nm) as shown in Figure 3.4. The 20.47 mm long grating consisted of 7 turns packed into an area of $\approx 0.57mm^2$. The corner bend radii were set to 100 μm and the gap between one grating post and strip waveguide in the corners was adjusted with a view to keeping the grating unchirped in the bends.
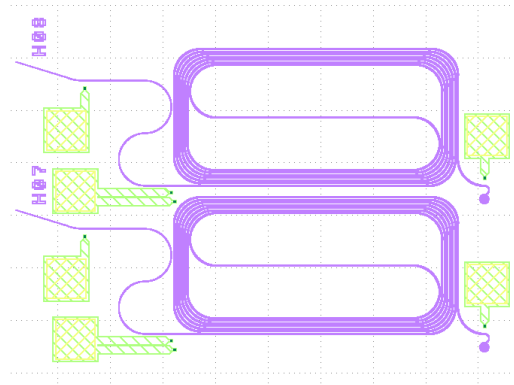
Figure **3.4** *Rectangular DBR mask layout, showing the packed strip waveguides and input tapers (purple) as well as phase shifters (yellow)*

3.3   EME Simulations

The commercial photonic simulator Ansys Lumerical's Eigen-mode expansion (EME) solver [104] was used for the purposes of simulating the spectral response of integrated DBRs. The computational cost of the solver scales well with the device length, making it more efficient compared to FDTD-based solvers for the design

and optimization of long periodic devices like DBRs. The solver methodology involves three steps:

1. First, the electromagnetic fields are decomposed into a basis set of eigenmodes. These modes are computed by dividing a single DBR period into multiple 'cells' in the longitudinal direction (see Figure 3.5) and then solving for the modes at the interface between adjacent cells (50 cells with 10 trial modes in our case). Scattering matrices for each section are then formulated by matching the tangential electric (E) and magnetic (H) fields at the cell boundaries.

2. Next, the solution to each section can be propagated bi-directionally to calculate the optical S-matrix of the entire device.

3. Finally, the DBR transmission/reflectivity spectrum can be obtained by performing a wavelength sweep using a perturbative method.
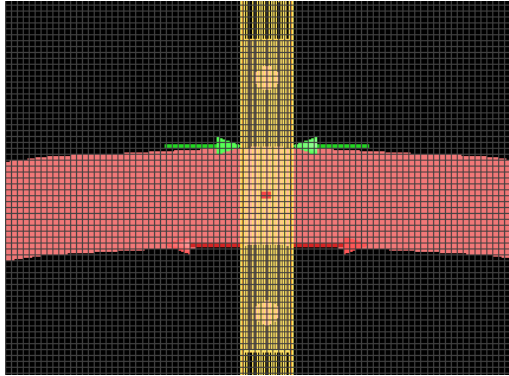
Figure 3.5 *EME simulation setup for one period of the cladding modulated DBR. Red: Si_3N_4 bent waveguide. Yellow: Cells in propagation direction. Green and red arrows: input and output ports for fundamental TE mode, respectively.*

3.3.1   2 µm Spiral DBR

The main challenge encountered when designing a grating on a spiral waveguide is that the effective refractive index n_{eff}, of the waveguide and consequently the Bragg wavelength λ_0 (from Eqn. 2.1), varies with the radius of curvature of the spiral. This effect can also be termed as chirping. In the fabricated rectangular spiral DBRs, the chirping was dealt with by compensating n_{eff} through a modification of the coupling gap in the bent sections, specifically from 865 nm to 1365 nm for the gap between outer post and strip waveguide. The propagation in these 20.47 mm long rectangular spiral DBRs was simulated first of all. In order to understand

the contribution of bends in the overall response, we compared the spectra resulting from a long straight DBR approximation, to a full simulation of the device containing seven rectangular spiral segments including the 100 μm radius bends. The propagation in the straight segments and bend segments were separately solved in EME and cascaded using the exported s-parameter models in Lumerical Interconnect, a commercial photonic circuit simulator [105]. Figure 3.6 shows the obtained reflectance spectra. In both cases the peak resonance is approximately at 2008 nm with an full-width half-maximum (FWHM) linewidth of 0.13 nm. There are only two noticeable differences. One, the side-lobe is stronger in the straight approximation and the side-mode suppression ratio (SMSR), defined as the transmission difference between the dominant transmission peak and the nearest side-peak, is smaller by about 1 dB . Two, the asymmetry in the full device simulation is due to the asymmetry of the outer and inner post gap distance in the bends. Therefore, the chirping in the 100 μm bends are well compensated by the post gap variation. The 6 nm shift in resonance compared to the target (2002 nm) is most likely due to inaccuracies in the Si$_3$N$_4$ refractive index data available for simulation.
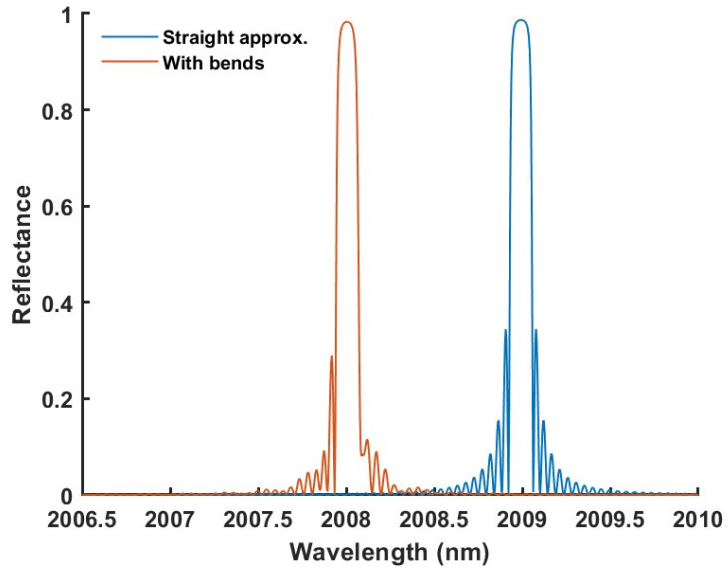
Figure 3.6 *Simulated reflectances of a rectangular spiral DBR, with and without straight waveguide approximation. Peak wavelength of second spectrum is shifted to 2009 nm for easier visual comparison.*

Next, a series of EME simulations were performed using the design parameters of the measured 2 μm circular spiral DBR with different bend radii to quantify how λ_0 shifts as the bend radius decreases. Figure 3.7 shows the simulated shift in resonance stays well within the target linewidth of 0.05 nm for the smallest bend radii (145 μm S-bends) and becomes negligible above bend radii of 200 μm. This feature,

coupled with the negligible bending losses, allows us to approximate the spiral as a long straight waveguide for simplified simulations. As visualized in Figure 3.8, the designed DBR length of 20 mm ($\approx$ 33800 periods) was chosen to meet the target FWHM linewidth (which improves with DBR length according to Eqn. 2.6) and SMSR. We noted that the actual laser SMSRs were much larger than the simulated SMSRs for the DBR cavity. The slight decrease of SMSR with DBR length is due to a disproportionate increase in side-lobe strength. It is common in practice to Gaussian-apodize Bragg gratings by varying the corrugation depth or post gaps to suppress the side-lobes [106].
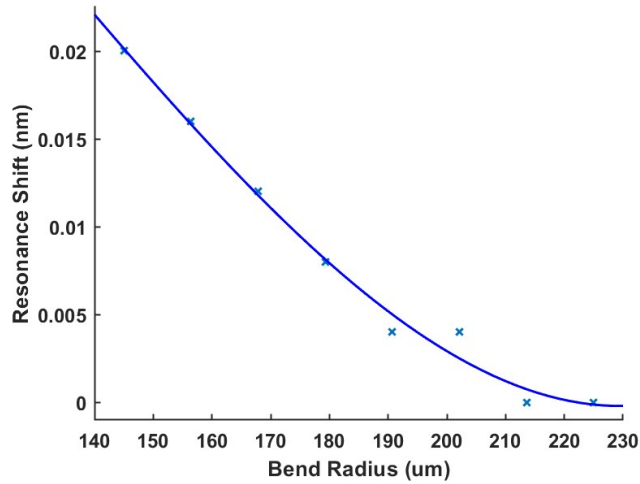
Figure **3.7** *Simulated shift in DBR resonance as a function of Si_3N_4 waveguide bend radius*
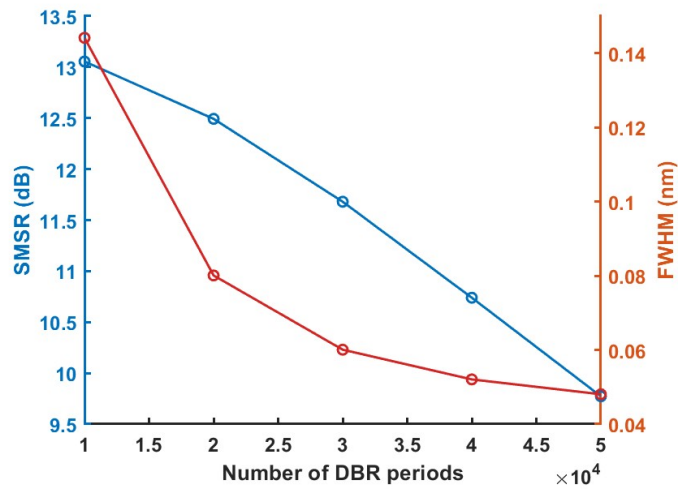
Figure **3.8** *Simulated side-mode suppression ratio (SMSR, left axis) and FWHM (right axis) as a function of number of periods or alternatively length of the DBR*

Figure 3.9 shows the simulated device response. We also simulated the one-post version of DBR to compare the reflection spectrum with the symmetric two-post design. The one post design features a narrower peak (FWHM of 0.06 nm vs. 0.092 nm) thanks to lower refractive index contrast or coupling strength, following Eqn. 2.6. It also demonstrates smaller side modes (SMSR is larger by 3.5 dB) at the expense of peak DBR reflectance. In practical terms, a one-post grating longer than 20 mm would be required to achieve the same target lasing threshold current or laser output. The peak reflectivity for the two-post case is slightly smaller than that of the rectangular spiral, due to a larger coupling gap (1000 nm vs. 865 nm) and slightly shorter (20 mm vs 20.47 mm) grating length, following the dependence in Eqn. 2.4.
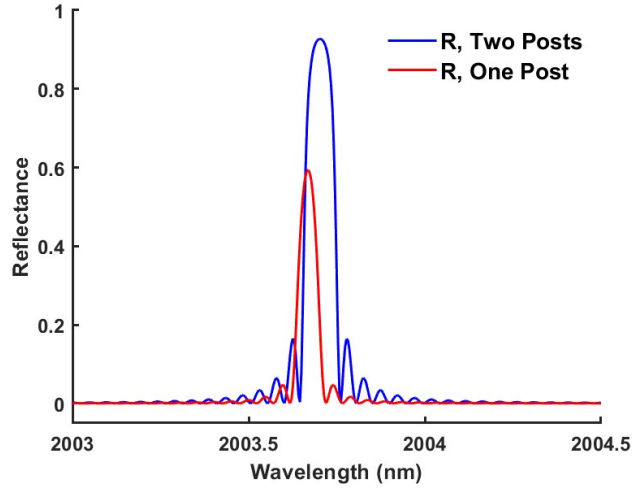
Figure 3.9 *Simulated device reflectance for one-post and two-post grating design*

As can be seen, the Bragg wavelength of the spectral response is 2003.67 nm for the grating period of 603.6 nm used in the simulations. To accommodate fabrication variations in the MPW process, we also varied the grating period by a pessimistic value of ± 2 nm, i.e., we simulated two other gratings with periods of approximately 601 nm and 605 nm. As shown in Figure 3.10, the Bragg wavelength blue-shifts as the grating period decreases and vice-versa, while the linewidths essentially remain the same. A look at Eqn. 2.1 might lead one to think that the shift should be symmetric and linear with change of periodicity. However, it must be remembered that n_{eff} is wavelength dependent and therefore the group index should also be taken into account.
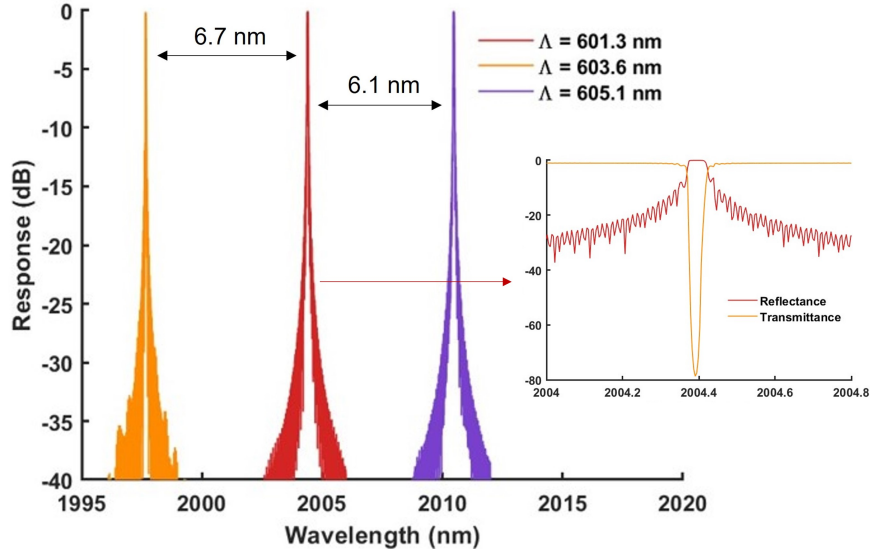
Figure 3.10 *Simulated reflectance spectra (in dB) for SBGW varying the period (keeping other parameters unchanged). Inset, zoomed response of 2004 nm DBR reflectance and transmittance in dB.*

3.3.2   2.7 µm Spiral DBR

For the 2.7 μm DBRs, a Bragg period of 823 nm and a Si$_3$N$_4$ waveguide width of 1.65 μm was selected, which is the largest width where single-mode operation is maintained over the 2.4–2.7 μm band [72]. The coupling gaps were kept the same. The reflectances of the individual spiral segments and the full device reflectance is shown in Figure 3.11. Though there is a 0.12 nm shift of the peak for the 145 μm S-bend, it fails to make a sizeable perturbation on the overall device response due to the low number of grating periods, which scales with the bend radius as $2\pi R_{bend}/\Lambda$. The overall device response is within the target linewidth of ≈ 0.4 nm, close to the experimental result in [107].

Next, a further sweep of the bend radius (R_{bend}) was carried out to explore the feasibility of more tightly packed spirals. For bends longer than 290 μm, the effective index variation (δn_{eff}) is very small, so compensations were unnecessary for the fabricated devices. As can be observed in Figure 3.12(a), the chirping is non-negligible for bends tighter than 180 μm. So we tried to compensate the δn_{eff} by varying the coupling gap of the inner-side posts (keeping the other post unchanged) and Figure 3.12(b) shows the effect of this. Eqn. 2.4 predicts that a smaller coupling coefficient resulting from a larger coupling gap weakens the peak reflectivity as a side-effect. Theoretically, such a small δn_{eff} can also be compensated for by an
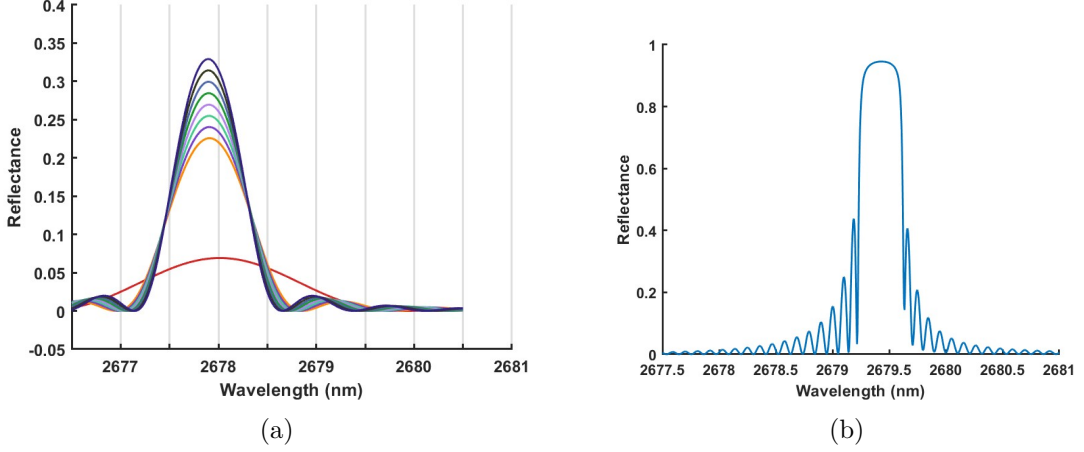
Figure 3.11 *(a) Simulated reflectance spectrum for DBR S-bend (red) and individual spiral segments with bend radii from 290 µm (orange) to 370 µm (dark blue) (b) Simulated reflectance spectrum of full grating using Lumerical Interconnect, demonstrating a linewidth < 0.4 nm.*

appropriate change of the grating period (Λ) based on Eqn. 2.1, from which follows:

$$n_{eff,c}\Lambda_c = n_{eff}\Lambda \tag{3.1}$$

Figure 3.13(a) shows the resonance shift behaviour for a uniform SBGW, a coupling
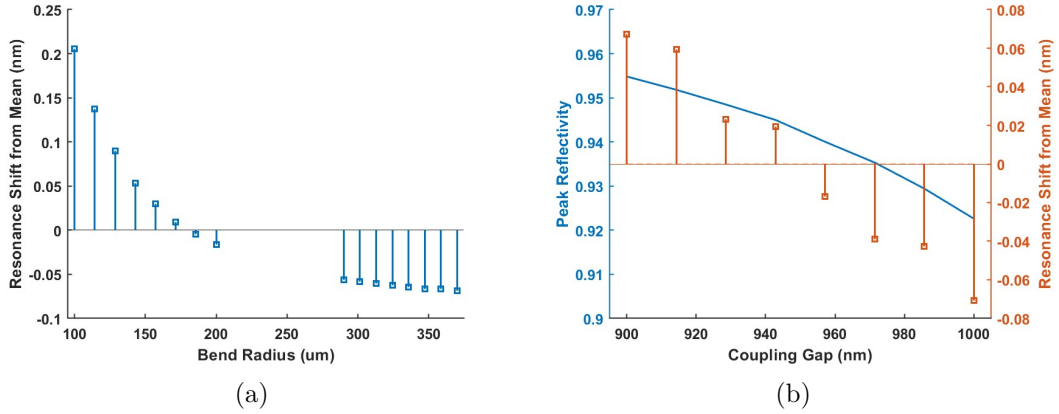
Figure 3.12 *Quantifying the resonance shift and reflectivity with varying (a) bend radii and (b) coupling gap in spirals*

gap varied SBGW, and a period varied SBGW. The coupling gap is for the inner posts is varied from 900 to 1000 nm and the period is varied around $\Lambda \pm 0.05$ nm. Period compensation only slightly outperforms gap compensation for spirals with bend radii between 100 and 200 µm. Ultimately, Figure 3.13(b) shows that the sim-

ulated spectrum is not greatly affected by the small value of δn_{eff}; in fact, coupling gap compensation causes a linewidth increase of about 20% and an asymmetry in the response when using unequal post gaps. Practically however, it is easier to vary the gap while such small variations in the grating period is difficult to resolve in the MPW process [54].
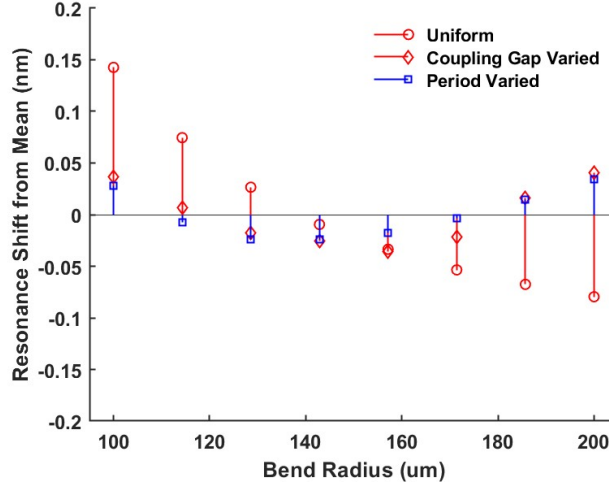
(a)
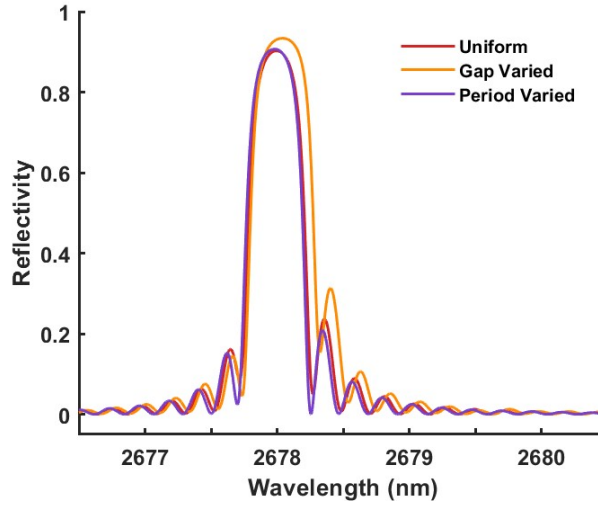
(b)

Figure 3.13 *Results of coupling gap and period compensation for the (a) resonance shift and (b) SBGW reflectivity spectrum with linewidths of approximately 0.4 nm*

4 Experimental Results and Discussion

In this chapter, we discuss the characterization of the used gain chip, present the waveguide alignment and measurement setup, and finally discuss the performance of hybrid lasers at 2 μm built using multiple PICs from the same MPW. The measurements are interpreted with the understanding gained from the simulations and give insight into process variation and design reliability.

4.1 RSOA Characterization

To determine the output power of the hybrid laser, we must first know the amplified spontaneous emission (ASE) output power from the rear facet of the RSOA. The RSOA was affixed with the p-side facing downward onto an AlN submount to enhance heat dissipation within the active region, thereby optimizing efficiency. This AlN submount was positioned onto a copper heatsink for characterization purposes. Power calibration was achieved by measuring the power output of a well-known device using an integrating sphere setup. In this setup, the device's output was directed into an integrating sphere, and a photodetector was placed at one of its outputs. Subsequently, the ASE output power from the rear facet of the RSOA was measured using the same configuration, with pulsed current injection at a frequency of 100 kHz and a duty cycle of 10% to minimize heating effects, as illustrated in Figure 4.1. A maximum ASE average power of almost 2 mW is observed at an injection current of 610 mA. Thermal rollover occurs at currents >650 mA as the output power falls off due to increased thermal losses.

We coupled the output of the RSOA to a Fourier transform infrared spectrometer (FTIR) via a multi-mode fiber and measured the ASE spectrum at constant currents of 200 mA and 300 mA. The maximum spectral intensity is at ≈1.96 μm, while the full-width half maximum (FWHM) is about 90 nm. The location of the RSOA gain maximum depends on the temperature of the active region, which can be adjusted by changing the duty cycle of the current injection.
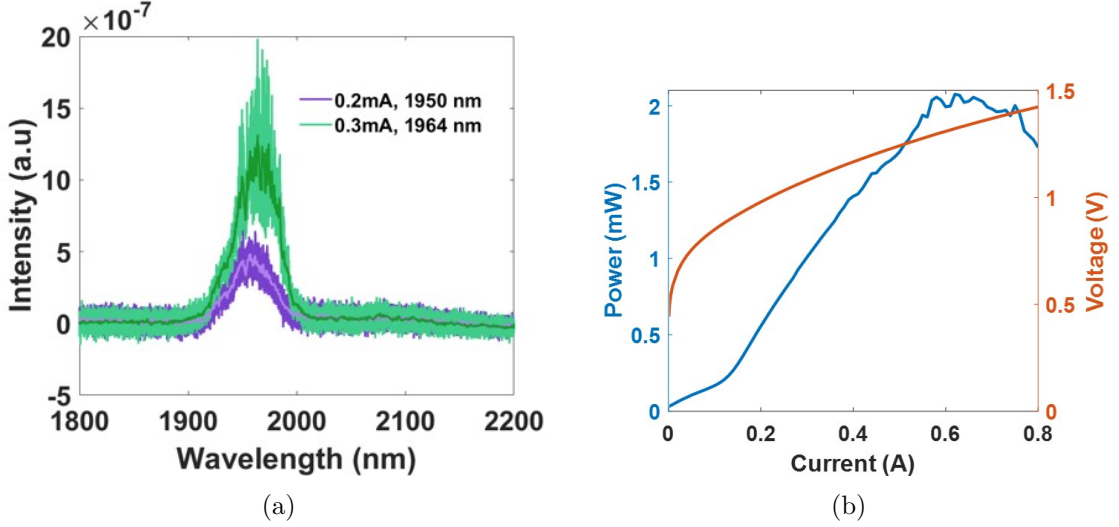
Figure 4.1 *(a) The ASE spectrum of the RSOA and (b) the average output power of the RSOA as a function of injection current pulse amplitude, from rear facet*

4.2 Alignment and Measurement Setup

Alignment of a 400 nm wide and 800 nm thick SNOI taper input with a 5 μm wide and 2 μm thick RSOA ridge waveguide was the necessary task. Figure 4.2 shows the home-built alignment setup which typically consists of a laser source, optical power sensors, fibers, and stages. The RSOA was placed p-side down on an AlN submount on a heatsink attached to a rotation stage, and the PIC was placed on an uncooled Thorlabs 3-Axis NanoMax stage controlled with Thorlabs Piezo Controllers and Strain Gauge Readers. A cleaved and stripped multi-mode ZrF fiber was aligned at the rear facet of the RSOA, purposefully brought in at an angle to prevent parasitic reflections from the fiber end to the laser cavity. The other end of the optical fiber was connected to a photodetector (PD) using an optical chopper operating at a chopping frequency of 300 Hz. A CW injection around the laser threshold current was provided to the RSOA through probe needles placed on its contacts. The signal magnitude received by the photodetector was measured using an SR810 Lock-In Amplifier, synchronized with the trigger signal from the optical chopper. To align the waveguides within the RSOA and the PIC, a 2D piezo scan was performed in a closed-loop configuration. This scan was carried out using a rotation stage and a 3-axis stage. The goal was to find the position that maximized the signal received by the photodetector. The coupling gap (in the x-direction) between the RSOA and the PIC was adjusted manually using differential adjusters, while the horizontal (y-direction) and vertical (z-direction) positions were optimized during the 2D raster scan by programming the piezo controllers.
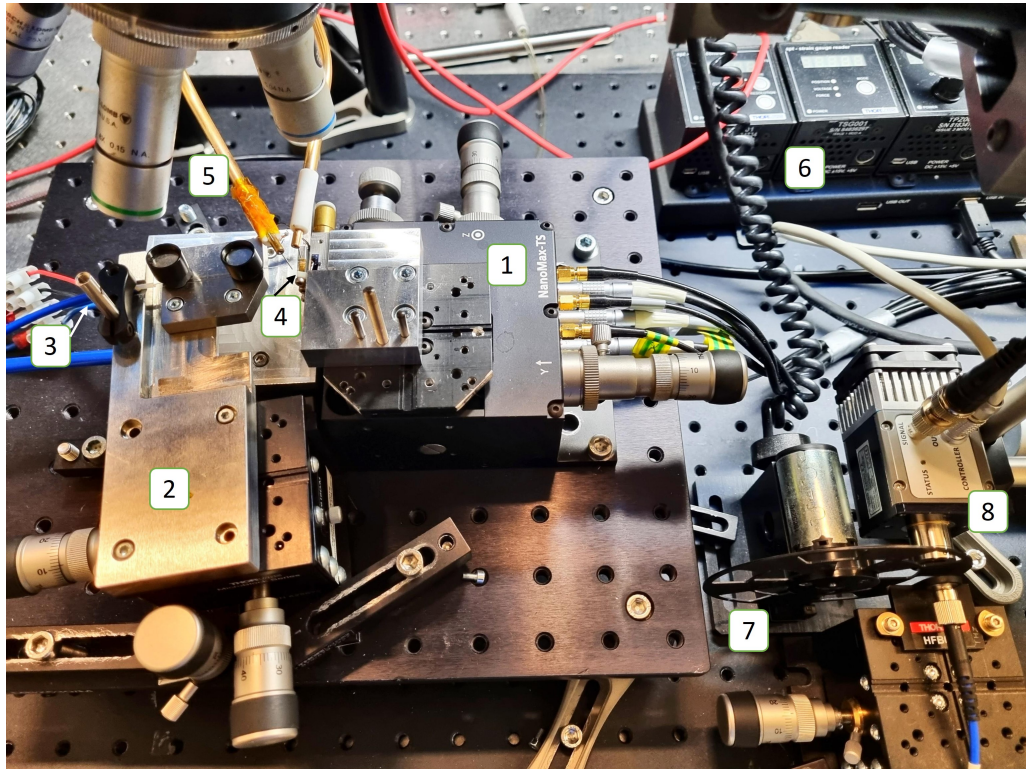
(a) Top view of the alignment and measurement setup: 1. Chip alignment stage   2. Fiber stage   3. Multimode fiber   4. RSOA heatsink   5. Injection probe needles   6. Piezo controller   7. Optical chopper   8. Photodetector
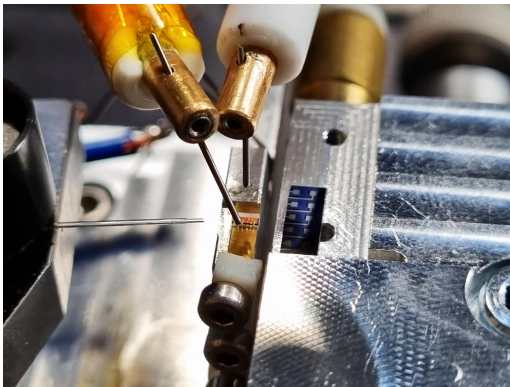
(b) Stripped fiber, RSOA and PIC
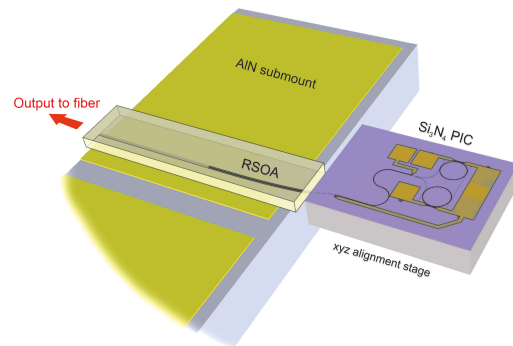
(c) Schematic of the gain chip and PIC alignment showing the RSOA waveguide at the bottom of the chip and Si_3N_4 on the top

Figure 4.2 *Setup photos and schematic*

Initially the z axis was roughly aligned visually by keeping the PIC and RSOA contact focused together in the microscope, since the waveguide for a p-down RSOA is located towards the bottom. Figure 4.3 shows the 2D plot of the piezo scan done near the optimum position. The alignment accuracy achieved was within a <10 nm range, limited by the piezo controllers. The alignment gap between the RSOA and

PIC was approximately 1 μm, set by the accuracy of the differential adjuster and the optical microscope resolution.
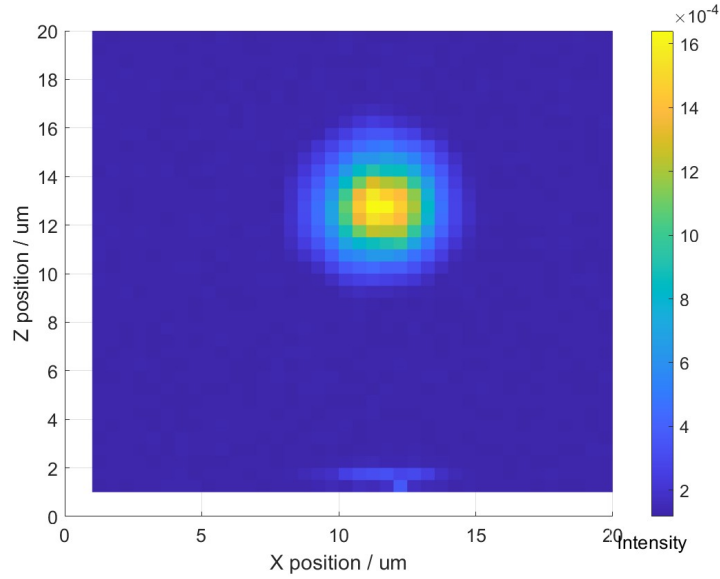
Figure 4.3 *Plot of a 2D piezo scan of the PIC along the y and z axes. Color indicates the intensity of the signal measured with the photodiode.*

4.3 Integrated Laser Performance

After the optimum alignment was achieved, the light-current (LI) curves were measured by sweeping CW current (i.e. 100% duty cycle) from 0 to 600 mA (upper limit chosen as per RSOA thermal rollover) into the RSOA and recording the signal level with the lock in amplifier. CW current is recommended for spectrum measurements. When using pulsed current, the injection current changes in time, heating the RSOA and thermo-optically changing its phase, thus broadening the linewidth. That is, the phase also pulses and can lock at lower currents.

The spectra of the lasers were examined using a fast Fourier transform infrared (FTIR) Bristol Instruments 771 Spectrum Analyzer with sample averaging. After applying constant current near threshold obtained from the LI curves, running the micro-alignment script again and manually tuning the current to achieve a good phase match, the spectrum measurements provided the best signal level and minimum linewidth.

4.3.1 Rectangular Spiral DBR Lasers

The two hybrid laser cavities have a threshold current of 150 mA and 190 mA and reach a maximum CW output power of 12.9 mW for 396 mA and 17.6 mW

for 445 mA current respectively (Figure 4.4). Kinks in the laser power correspond to longitudinal 'mode hopping' commonly observed in DBR lasers [108]. As the current is increased, heating of the RSOA active region varies its refractive index through the thermo-optic effect. This leads to a current-dependent phase change in the RSOA while the phase of the PIC remains constant. At minimum phase-match between the RSOA and PIC, the lasing mode is detuned from the grating peak, which reduces the output power until eventually, the lasing mode hops to the next longitudinal mode. These mode hops are more common and of larger magnitude at higher currents, because Joule heating is more significant at high currents. It is also because the peak of the RSOA gain is red-shifted closer to the DBR resonance as the laser is heated, increasing the gain. The measured thermal rollover characteristic beginning around 590 mA can be delayed using pulsed instead of CW current, thus enabling higher peak power levels.

A cleaner and continuous single-mode output can be obtained by tuning the laser cavity for optimum phase match with a voltage controlled phase shifter available on the Si_3N_4 waveguide. Our used RSOA was left as-cleaved on both ends, though it is common to use an anti-reflection coating (ARC) on the front facet to maximize output coupling and broaden the obtainable spectrum by suppressing lasing. However, multi-layer ARCs add to the fabrication complexity. The rear facet can also be high-reflectance coated (HRC) to minimize mirror losses (R>90% from 1.9 μm to 2.05 μm) and lower the lasing threshold. The trade-off is that this scheme decreases average power output by a factor of 2 to 3 [27].
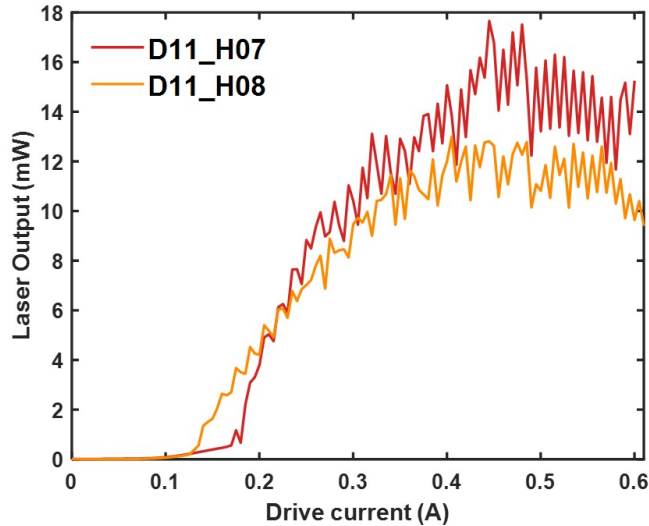
Figure 4.4 *Measured output power of the uncooled rectangular spiral DBR hybrid lasers at different CW injection currents*

Figure 4.5 shows that the lasing intensity on average peaks at 1987.71 nm and

1997.81 nm for the two cavities, about a (-)4.3 nm shift from design values. The SMSRs are about 25 dB and 26.6 dB and the measured FWHM linewidths is below 0.1 nm, both measurements limited by the 0.05 nm resolution of the FTIR spectrometer. The side lobes of the grating spectra are not fully symmetric as was observed in the simulation results, which is likely due to the slight grating post size variation (on the order of nm) along the long grating length (20.5 mm). There was no measurable spectral shift upon changing the RSOA current, exemplifying that DBRs are quite selective and insensitive to thermal shifts.
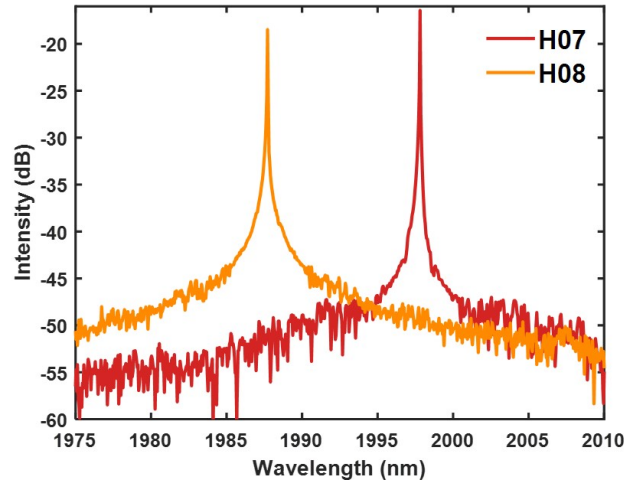
Figure 4.5 Fiber-coupled spectrum of the rectangular spiral DBR hybrid lasers measured at a CW RSOA current of 180 mA

4.3.2 Round Spiral DBR Lasers

Figure 4.6(a,b) shows the LI curve and spectrum for the PIC exhibiting maximum CW output power out of the 7 tested round spiral DBR lasers (H02 cavity), which exhibits about 16 mW at a current of 520 mA, and an SMSR of 22 dB at a peak wavelength of 1997.6 nm. The $\sim$6 nm shift in wavelength compared to the design ($\sim$2004 nm) is most likely due to inaccuracies in the Si_3N_4 refractive index data available for simulation, or the systematic geometrical errors in DBR thickness and lateral dimensions. An important observation in the LI data is a peculiar double current threshold behaviour. A first knee in the laser output is located at 150 mA and a steeper second one at 300 mA. Measurements of the spectra at lower currents revealed wavelength locking at around 1986 nm, although much weaker in signal intensity ($\sim$10 dB) and giving way to the main peak at the 'second' threshold current. This false peak is the probable explanation for this behaviour and may be verified by spectral reflectance measurements for the DBR. It is expected that at

lower currents, where current or gain tuning is not strong enough, using thermally tuned heaters available on the PIC for phase tuning can help the laser to lock into the nominal resonance wavelength and remove the second knee in the LI.
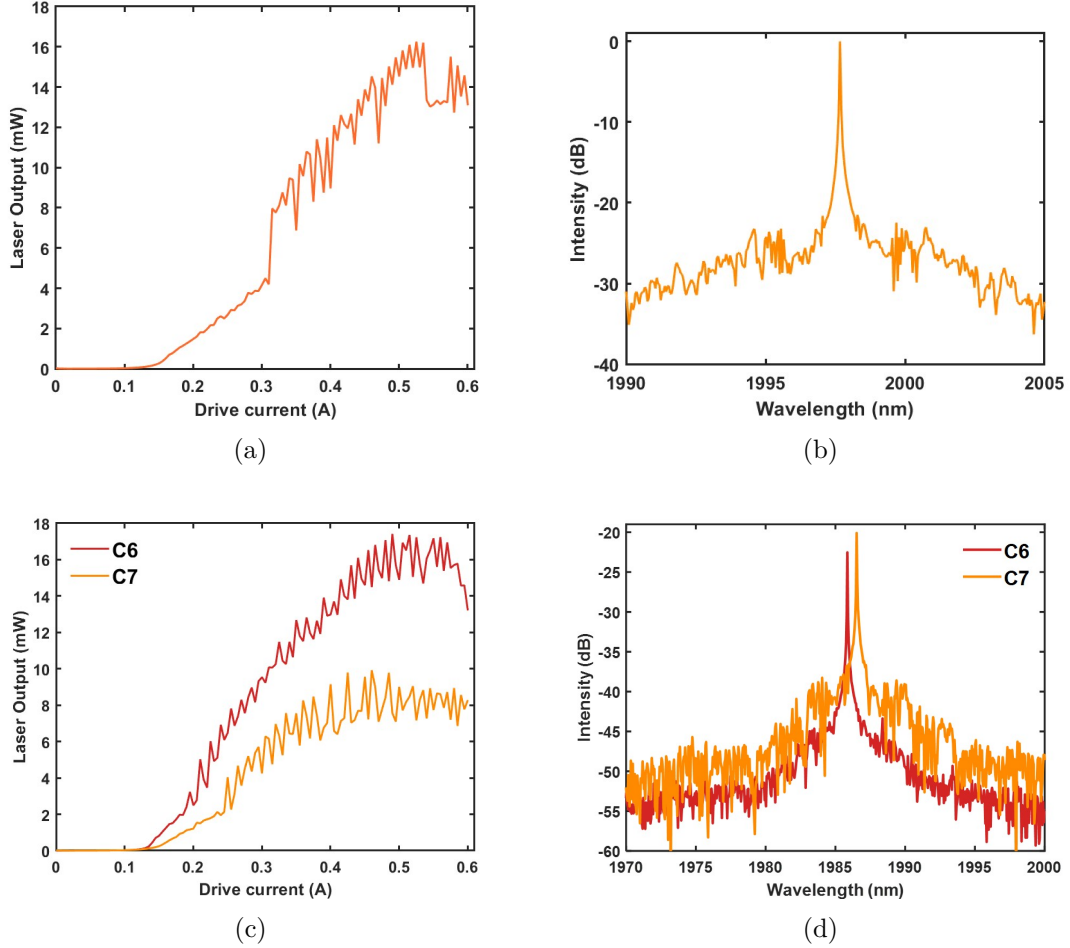
Figure   4.6 *(a) LI curve and (b) spectrum (measured at 200 mA CW current) of an uncooled round spiral DBR laser designed for 2004 nm emission. (c) LI curve and (d) spectrum (measured at 230 mA and 275 mA CW) of uncooled round spiral DBR lasers designed for 1994 nm*

To characterize the shorter wavelength (1994 nm) H01 cavities, two of the PICs were aligned and measured, and the results are shown in Figure 4.6(c,d). The lasers exhibits a threshold current of 185 mA and 240 mA, reaching a maximum output power of 17.4 mW (at 490 mA) and 9.9 mW (at 460 mA) respectively. The double threshold behaviour observed in the H02 cavities was not repeated here, and the thresholds were on average 30% smaller. The lasing wavelengths were at 1985.86 nm and 1986.52 nm with an SMSR of 19.5 dB and 16.5 dB respectively. We noted that the SMSR measurement was limited by the FTIR, where the spectrum was averaged over 5 measurements. The RSOA to fiber coupling was also not ideal for

large peak powers due to angled alignment of the fiber. The lasing wavelengths correspond to an approximate -0.5% deviation from design values. The measured FWHM linewidths were below 0.1 nm at all currents, limited by the FTIR resolution.

Comparing DBR wavelengths between the seven PICs at the H02 cavity (Figure 4.7), we see that the laser is able to achieve the targeted wavelength accuracy. There is a standard deviation of roughly 1 nm in the center wavelengths, which lie between 1995.74 nm and 1998.77 nm. It is to be noted that the observed wavelength variation can be easily dealt with using tuners, as exhibited in [28]. With respect to power consumption, the lasing thresholds are between 300 to 340 mA and peak powers are between 8 and 16 mW, while thermal rollover mostly begins around 530 mA of injection current. The variation of the achieved SMSRs (between 16 and 22 dB) clearly show the dependence of laser performance on the achieved alignment accuracy between the PIC and RSOA waveguides. Compared to the rectangular spirals, the SMSR is also lower due to a larger coupling gap (1000 nm vs. 865 nm) causing lower peak reflectivities following Eqn. 2.4 and simulation results. However, the linewidths should also be smaller for the same reason. The alignments were performed close to threshold currents as we mentioned, though theoretically the mode profile changes on the nm-scale and hence the achieved coupling quality is also a function of RSOA current or temperature. We noted this as a limitation of butt-coupled testing methods as compared to other hybrid integration methods, however it wasn't a goal of ours to maximize attainable output powers.
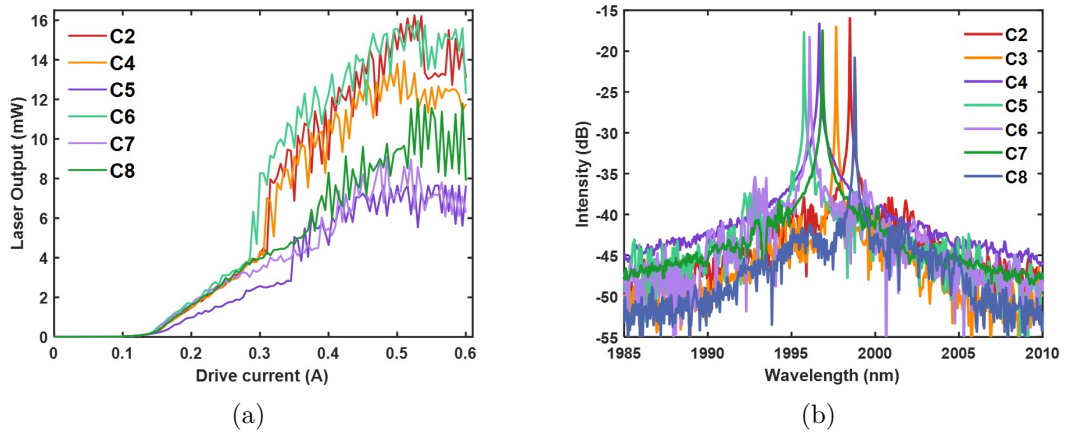
Figure 4.7 *Comparing (a) LI curves and (b) spectrum between seven different PICs manufactured in the same MPW run. N.B: LI measurements missing for C3 chip.*

It is important to note that proper linewidth measurement for the hybrid laser was not possible due to the FTIR's constrained resolution and mechanical instability of the contact probe needles, which creates noise in the emission wavelength. From the obtained FTIR spectra, the linewidth is estimated to be smaller than 0.05 nm.

The linewidth of the 1.99 μm laser was precisely determined using a heterodyne measurement technique in a co-authored publication [107] with a frequency comb phase-locked to an ultra-stable clock laser. Averaging the RF spectrum data over a stable 7 ms time window resulted in a linewidth of 49.6 kHz, while a 0.5 ms window achieved an 8 kHz-level linewidth.

5 Conclusion and Future Scope

This research was focused on contributing a reliable simulation framework and rapid testing methodology for narrow linewidth hybrid integrated lasers enabled by combining a versatile GaSb multi-quantum well gain chip technology with SNOI external cavities. Starting at verifying and optimizing the design of integrated Bragg gratings through numerical simulations, we used a commercial eigen-mode expansion solver using the design parameters of the fabricated 2 μm rectangular and circular spiral DBRs with different bend radii to quantify the shift of the resonance wavelength with decreasing bend radius. Approximating the circular spiral as a long straight waveguide, the simulations allowed us to design DBR lengths and corrugation parameters to meet linewidth and SMSR targets. In the case of 2.7 μm spirals, non-negligible chirping due to tight waveguide bends led us to propose a grating coupling gap and period compensated design to retain narrow reflectance spectra, which have been successfully demonstrated in practice using similar designs [28].

In the next step, the work progressed to tackling the real-world challenges related to integrated laser alignment and performance evaluation at mid-IR wavelengths. A low-loss SNOI platform permitted DBR lasers emitting in the range of 6-18 mW of CW power at $\sim$2 μm, with SMSRs of upto 26 dB. The lasers were operated with CW injection currents for optimum spectral measurements, and near threshold to prevent heating effects in uncooled conditions. The measured thresholds varied from 170 mA on average for rectangular spiral DBRs to 320 mA for circular spiral DBRs and can be improved by HR coating the as-cleaved output facet. It is appropriate to interpret our results in perspective of another SNOI-based 2 μm tunable Vernier external cavity laser recently reported in [13] which achieved a comparable CW output power of 15 mW, a threshold current of 100 mA, and an SMSR of about 20 dB across a tuning range of 90 nm around 2 μm. We note that these metrics were obtained with thermo-electric cooling of the RSOA at 23°C in contrast to our uncooled setup. This feature of relatively high power lasing enabled by the low-loss SNOI platform promises to be particularly advantageous in sensing applications, as it reduces the signal-to-noise ratio (SNR) leading to improved sensitivity and accurate measurement of smaller gas concentrations.

Testing of seven different PICs from the same MPW run resulted in narrow linewidth lasing between 1995.7 nm and 1998.8 nm with a standard deviation of roughly 1 nm, demonstrating satisfactory tolerance to fabrication variation. The resonance wavelengths were blue-shifted roughly 7 nm from the design for all the cavities, pointing to a systematic error in the DBR periodicity or lateral dimensions. The choice of cladding modulation for the Bragg grating as opposed to common

periodic corrugation designs resulted in linewidths which could be estimated to be below 50 pm due to limited FTIR resolution, but measured to be in the sub-10 kHz regime using heterodyne measurements in a published work [107]. Using the simulation results from this work, it is expected that development of these lasers towards even narrower linewidths are possible, for example by utilising single-post grating designs.

The chosen hybrid integration method of butt-coupling allows for rapid and efficient prototyping compared to bonding methods and heterogeneous methods still in the maturing phase for GaSb. However, from the measured LI performance curves it is clear that the manually achieved alignment accuracy or in other words, the coupling loss, between the PIC and RSOA waveguides strongly dictate the peak powers and SMSR achievable, and somewhat the threshold currents. In terms of integration experiments for future study, the waveguides can be actively aligned, and the components cured together using UV curable adhesive. We expect that use of the thermal tuners on the DBR will help with ameliorating the double threshold characteristic in the LI and obtaining cleaner laser outputs. Demonstration of the tunability of the lasing wavelength is the obvious next step to complete the laser characterization and establish its readiness for spectroscopic sensing applications. Optimization of the inverse taper and applying ARC coating on the PICs is also a strong direction for reducing the coupling loss and consequently the thresholds. This thesis sets the baseline for the modelling and characterization of such devices with the expectation that on-chip integration of the RSOA and packaging of the hybrid laser will significantly enhance its performance in terms of threshold current, output power and spectral purity.

References

[1] J. F. Bauters, M. J. R. Heck, D. John, *et al.*, "Ultra-low loss silica-based waveguides with millimeter bend radius," in *36th European Conference and Exhibition on Optical Communication*, 2010, pp. 1–3. DOI: `10.1109/ECOC.2010.5621341`.

[2] C. Doerr, "Silicon photonic integration in telecommunications," *Frontiers in Physics*, vol. 3, 2015, ISSN: 2296-424X. DOI: `10.3389/fphy.2015.00037`. [Online]. Available: `https://www.frontiersin.org/articles/10.3389/fphy.2015.00037`.

[3] S. Dhall, B. Mehta, A. Tyagi, and K. Sood, "A review on environmental gas sensors: Materials and technologies," *Sensors International*, vol. 2, p. 100 116, 2021, ISSN: 2666-3511. DOI: `https://doi.org/10.1016/j.sintl.2021.100116`. [Online]. Available: `https://www.sciencedirect.com/science/article/pii/S2666351121000371`.

[4] K. Scholle, S. Lamrini, P. Koopmann, and P. Fuhrberg, "2 μm laser sources and their possible applications," in *Frontiers in Guided Wave Optics and Optoelectronics*, B. Pal, Ed., Rijeka: IntechOpen, 2010, ch. 21. DOI: `10.5772/39538`. [Online]. Available: `https://doi.org/10.5772/39538`.

[5] F. Han, T. Wang, G. Liu, *et al.*, "Materials with tunable optical properties for wearable epidermal sensing in health monitoring," *Advanced Materials*, vol. 34, no. 26, p. 2 109 055, 2022. DOI: `https://doi.org/10.1002/adma.202109055`. eprint: `https://onlinelibrary.wiley.com/doi/pdf/10.1002/adma.202109055`. [Online]. Available: `https://onlinelibrary.wiley.com/doi/abs/10.1002/adma.202109055`.

[6] N. V. Alexeeva and M. A. Arnold, "Near-infrared microspectroscopic analysis of rat skin tissue heterogeneity in relation to noninvasive glucose sensing," *Journal of Diabetes Science and Technology*, vol. 3, no. 2, pp. 219–232, 2009, PMID: 20144353. DOI: `10.1177/193229680900300202`. eprint: `https://doi.org/10.1177/193229680900300202`. [Online]. Available: `https://doi.org/10.1177/193229680900300202`.

[7] D. Popa and F. Udrea, "Towards integrated mid-infrared gas sensors," *Sensors*, vol. 19, no. 9, p. 2076, 2019.

[8] G. Roelkens, L. Liu, D. Liang, *et al.*, "Iii-v/silicon photonics for on-chip and intra-chip optical interconnects," *Laser & Photonics Reviews*, vol. 4, no. 6, pp. 751–779, 2010. DOI: `https://doi.org/10.1002/lpor.200900033`. eprint: `https://onlinelibrary.wiley.com/doi/pdf/10.1002/lpor.`

200900033. [Online]. Available: https://onlinelibrary.wiley.com/doi/abs/10.1002/lpor.200900033.

[9] Z. Wang, A. Abbasi, U. Dave, *et al.*, "Novel light source integration approaches for silicon photonics," *Laser & Photonics Reviews*, vol. 11, no. 4, p. 1 700 063, 2017. DOI: https://doi.org/10.1002/lpor.201700063. eprint: https://onlinelibrary.wiley.com/doi/pdf/10.1002/lpor.201700063. [Online]. Available: https://onlinelibrary.wiley.com/doi/abs/10.1002/lpor.201700063.

[10] C. Lin, M. Grau, O. Dier, and M.-C. Amann, "Low threshold room-temperature continuous-wave operation of 2.24–3.04 m GaInAsSb/AlGaAsSb quantum-well lasers," *Applied Physics Letters*, vol. 84, no. 25, pp. 5088–5090, Jun. 2004, ISSN: 0003-6951. DOI: 10.1063/1.1760218. eprint: https://pubs.aip.org/aip/apl/article-pdf/84/25/5088/14317412/5088_1_online.pdf. [Online]. Available: https://doi.org/10.1063/1.1760218.

[11] K. Vizbaras and M.-C. Amann, "Room-temperature 3.73 µm gasb-based type-i quantum-well lasers with quinternary barriers," *Semiconductor Science and Technology*, vol. 27, no. 3, p. 032 001, Jan. 2012. DOI: 10.1088/0268-1242/27/3/032001. [Online]. Available: https://dx.doi.org/10.1088/0268-1242/27/3/032001.

[12] R. Wang, A. Malik, I. Šimonytė, A. Vizbaras, K. Vizbaras, and G. Roelkens, "Compact gasb/silicon-on-insulator 2.0x μm widely tunable external cavity lasers," *Opt. Express*, vol. 24, no. 25, pp. 28 977–28 986, Dec. 2016. DOI: 10.1364/OE.24.028977. [Online]. Available: https://opg.optica.org/oe/abstract.cfm?URI=oe-24-25-28977.

[13] N. Zia, S.-P. Ojanen, J. Viheriala, *et al.*, "Widely tunable 2 um hybrid laser using gasb semiconductor optical amplifiers and a si3n4 photonics integrated reflector," *Opt. Lett.*, vol. 48, no. 5, pp. 1319–1322, Mar. 2023. DOI: 10.1364/OL.480867. [Online]. Available: https://opg.optica.org/ol/abstract.cfm?URI=ol-48-5-1319.

[14] S.-P. Ojanen, J. Viheriälä, M. Cherchi, *et al.*, "GaSb diode lasers tunable around 2.6 m using silicon photonics resonators or external diffractive gratings," *Applied Physics Letters*, vol. 116, no. 8, p. 081 105, Feb. 2020, ISSN: 0003-6951. DOI: 10.1063/1.5140062. [Online]. Available: https://doi.org/10.1063/1.5140062.

[15] P. Kaur, A. Boes, G. Ren, T. G. Nguyen, G. Roelkens, and A. Mitchell, "Hybrid and heterogeneous photonic integration," *APL Photonics*, vol. 6, no. 6, 2021.

[16]   C. Xiang, J. Liu, J. Guo, *et al.*, "Laser soliton microcombs heterogeneously integrated on silicon," *Science*, vol. 373, no. 6550, pp. 99–103, 2021.

[17]   C. O. de Beeck, B. Haq, L. Elsinger, *et al.*, "Heterogeneous iii-v on silicon nitride amplifiers and lasers via microtransfer printing," *Optica*, vol. 7, no. 5, pp. 386–393, May 2020. DOI: `10.1364/OPTICA.382989`. [Online]. Available: `https://opg.optica.org/optica/abstract.cfm?URI=optica-7-5-386`.

[18]   Y. Guo, R. Zhao, G. Zhou, *et al.*, "Thermally tuned high-performance iii-v/si 3 n 4 external cavity laser," *IEEE Photonics Journal*, vol. 13, no. 2, pp. 1–13, 2021.

[19]   Y. Fan, A. van Rees, P. J. M. van der Slot, *et al.*, "Hybrid integrated inp-si3n4 diode laser with a 40-hz intrinsic linewidth," *Opt. Express*, vol. 28, no. 15, pp. 21 713–21 728, Jul. 2020. DOI: `10.1364/OE.398906`. [Online]. Available: `https://opg.optica.org/oe/abstract.cfm?URI=oe-28-15-21713`.

[20]   E. Vissers, S. Poelman, C. O. de Beeck, K. Van Gasse, and B. Kuyken, "Hybrid integrated mode-locked laser diodes with a silicon nitride extended cavity," *Optics Express*, vol. 29, no. 10, pp. 15 013–15 022, 2021.

[21]   P. Muñoz, G. Micó, L. A. Bru, *et al.*, "Silicon nitride photonic integration platforms for visible, near-infrared and mid-infrared applications," *Sensors*, vol. 17, no. 9, 2017, ISSN: 1424-8220. DOI: `10.3390/s17092088`. [Online]. Available: `https://www.mdpi.com/1424-8220/17/9/2088`.

[22]   C. Xiang, P. A. Morton, and J. E. Bowers, "Ultra-narrow linewidth laser based on a semiconductor gain chip and extended si3n4 bragg grating," *Opt. Lett.*, vol. 44, no. 15, pp. 3825–3828, Aug. 2019. DOI: `10.1364/OL.44.003825`. [Online]. Available: `https://opg.optica.org/ol/abstract.cfm?URI=ol-44-15-3825`.

[23]   W. Jin, Q.-F. Yang, L. Chang, *et al.*, "Hertz-linewidth semiconductor lasers using cmos-ready ultra-high-q microresonators," *Nature Photonics*, vol. 15, no. 5, pp. 346–353, May 2021, ISSN: 1749-4893. DOI: `10.1038/s41566-021-00761-7`. [Online]. Available: `https://doi.org/10.1038/s41566-021-00761-7`.

[24]   [Online]. Available: `https://www.imec-int.com/en/what-we-offer/development/system-development-technologies/Integrated-photonics/silicon-nitride-based-photonics`.

[25]   B. Mroziewicz, "External cavity wavelength tunable semiconductor lasers - a review," *Opto-Electronics Review*, vol. 16, no. 4, pp. 347–366, Dec. 2008, ISSN: 1896-3757. DOI: `10.2478/s11772-008-0045-9`. [Online]. Available: `https://doi.org/10.2478/s11772-008-0045-9`.

[26] A. J. Zilkie, P. Seddighian, B. J. Bijlani, *et al.*, "Power-efficient iii-v/silicon external cavity dbr lasers," *Opt. Express*, vol. 20, no. 21, pp. 23 456–23 462, Oct. 2012. DOI: `10.1364/OE.20.023456`. [Online]. Available: `https://opg.optica.org/oe/abstract.cfm?URI=oe-20-21-23456`.

[27] N. Zia, H. Tuorila, J. Viheriälä, *et al.*, "Hybrid silicon photonics dbr laser based on flip-chip integration of gasb amplifiers and um-scale soi waveguides," *Opt. Express*, vol. 30, no. 14, pp. 24 995–25 005, Jul. 2022. DOI: `10.1364/OE.460883`. [Online]. Available: `https://opg.optica.org/oe/abstract.cfm?URI=oe-30-14-24995`.

[28] S.-P. Ojanen, J. Viheriälä, N. Zia, *et al.*, "Discretely tunable (2594, 2629, 2670 nm) gasb/si3n4 hybrid laser for multiwavelength spectroscopy," *Laser & Photonics Reviews*, vol. n/a, no. n/a, p. 2 300 492, DOI: `https://doi.org/10.1002/lpor.202300492`. eprint: `https://onlinelibrary.wiley.com/doi/pdf/10.1002/lpor.202300492`. [Online]. Available: `https://onlinelibrary.wiley.com/doi/abs/10.1002/lpor.202300492`.

[29] R. Wang, S. Sprengel, A. Vasiliev, *et al.*, "Widely tunable 2.3 μ iii-v-on-silicon vernier lasers for broadband spectroscopic sensing," *Photon. Res.*, vol. 6, no. 9, pp. 858–866, Sep. 2018. DOI: `10.1364/PRJ.6.000858`. [Online]. Available: `https://opg.optica.org/prj/abstract.cfm?URI=prj-6-9-858`.

[30] H. Subbaraman, X. Xu, A. Hosseini, *et al.*, "Recent advances in silicon-based passive and active optical interconnects," *Opt. Express*, vol. 23, no. 3, pp. 2487–2511, Feb. 2015. DOI: `10.1364/OE.23.002487`. [Online]. Available: `https://opg.optica.org/oe/abstract.cfm?URI=oe-23-3-2487`.

[31] E. H. Bernhardi, H. A. van Wolferen, L. Agazzi, *et al.*, "Ultra-narrow-linewidth, single-frequency distributed feedback waveguide laser in al2o3:er3+ on silicon," *Opt. Lett.*, vol. 35, no. 14, pp. 2394–2396, Jul. 2010. DOI: `10.1364/OL.35.002394`. [Online]. Available: `https://opg.optica.org/ol/abstract.cfm?URI=ol-35-14-2394`.

[32] M. Belt, T. Huffman, M. L. Davenport, W. Li, J. S. Barton, and D. J. Blumenthal, "Arrayed narrow linewidth erbium-doped waveguide-distributed feedback lasers on an ultra-low-loss silicon-nitride platform," *Opt. Lett.*, vol. 38, no. 22, pp. 4825–4828, Nov. 2013. DOI: `10.1364/OL.38.004825`. [Online]. Available: `https://opg.optica.org/ol/abstract.cfm?URI=ol-38-22-4825`.

[33] M. Smit, X. Leijtens, H. Ambrosius, *et al.*, "An introduction to inp-based generic integration technology," *Semiconductor Science and Technology*, vol. 29, no. 8, p. 083 001, Jun. 2014. DOI: 10.1088/0268-1242/29/8/083001. [Online]. Available: https://dx.doi.org/10.1088/0268-1242/29/8/083001.

[34] P. Muñoz, G. Micó, L. A. Bru, *et al.*, "Silicon nitride photonic integration platforms for visible, near-infrared and mid-infrared applications," vol. 17, no. 9, Sep. 2017. DOI: 10.3390/S17092088.

[35] D. J. Blumenthal, R. Heideman, D. Geuzebroek, A. Leinse, and C. Roeloffzen, "Silicon nitride in silicon photonics," *Proceedings of the IEEE*, vol. 106, no. 12, pp. 2209–2231, 2018. DOI: 10.1109/JPROC.2018.2861576.

[36] D. D'Agostino, G. Carnicella, C. Ciminelli, *et al.*, "Low-loss passive waveguides in a generic inp foundry process via local diffusion of zinc," *Optics express*, vol. 23, no. 19, pp. 25 143–25 157, 2015.

[37] K. M. Yoo, J. Midkiff, A. Rostamian, C.-j. Chung, H. Dalir, and R. T. Chen, "Ingaas membrane waveguide: A promising platform for monolithic integrated mid-infrared optical gas sensor," *ACS sensors*, vol. 5, no. 3, pp. 861–869, 2020.

[38] M. Smit, K. Williams, and J. van der Tol, "Past, present, and future of InP-based photonic integration," *APL Photonics*, vol. 4, no. 5, p. 050 901, May 2019, ISSN: 2378-0967. DOI: 10.1063/1.5087862. eprint: https://pubs.aip.org/aip/app/article-pdf/doi/10.1063/1.5087862/14010749/050901_1_online.pdf. [Online]. Available: https://doi.org/10.1063/1.5087862.

[39] J. Bass, B. Brea, H. Tran, W. Du, R. Soref, and S.-Q. Yu, "The effect of two-photon absorption on the dynamic range of integrated microwave photonics links," in *Silicon Photonics XV*, SPIE, vol. 11285, 2020, pp. 216–223.

[40] R. Kitamura, L. Pilon, and M. Jonasz, "Optical constants of silica glass from extreme ultraviolet to far infrared at near room temperature," *Appl. Opt.*, vol. 46, no. 33, pp. 8118–8133, Nov. 2007. DOI: 10.1364/AO.46.008118. [Online]. Available: https://opg.optica.org/ao/abstract.cfm?URI=ao-46-33-8118.

[41] S. A. Miller, M. Yu, X. Ji, *et al.*, "Low-loss silicon platform for broadband mid-infrared photonics," *Optica*, vol. 4, no. 7, pp. 707–712, Jul. 2017. DOI: 10.1364/OPTICA.4.000707. [Online]. Available: https://opg.optica.org/optica/abstract.cfm?URI=optica-4-7-707.

[42] L. Zhuang, M. Hoekman, C. Taddei, *et al.*, "On-chip microwave photonic beamformer circuits operating with phase modulation and direct detection," *Opt. Express*, vol. 22, no. 14, pp. 17 079–17 091, Jul. 2014. DOI: `10.1364/OE.22.017079`. [Online]. Available: `https://opg.optica.org/oe/abstract.cfm?URI=oe-22-14-17079`.

[43] L. Zhuang, C. G. H. Roeloffzen, M. Hoekman, K.-J. Boller, and A. J. Lowery, "Programmable photonic signal processor chip for radiofrequency applications," *Optica*, vol. 2, no. 10, pp. 854–859, Oct. 2015. DOI: `10.1364/OPTICA.2.000854`. [Online]. Available: `https://opg.optica.org/optica/abstract.cfm?URI=optica-2-10-854`.

[44] Y. Okawachi, K. Saha, J. S. Levy, Y. H. Wen, M. Lipson, and A. L. Gaeta, "Octave-spanning frequency comb generation in a silicon nitride chip," *Opt. Lett.*, vol. 36, no. 17, pp. 3398–3400, Sep. 2011. DOI: `10.1364/OL.36.003398`. [Online]. Available: `https://opg.optica.org/ol/abstract.cfm?URI=ol-36-17-3398`.

[45] J. Chiles, N. Nader, D. D. Hickstein, *et al.*, "Deuterated silicon nitride photonic devices for broadband optical frequency comb generation," *Opt. Lett.*, vol. 43, no. 7, pp. 1527–1530, Apr. 2018. DOI: `10.1364/OL.43.001527`. [Online]. Available: `https://opg.optica.org/ol/abstract.cfm?URI=ol-43-7-1527`.

[46] J. P. Epping, T. Hellwig, M. Hoekman, *et al.*, "On-chip visible-to-infrared supercontinuum generation with more than 495 thz spectral bandwidth," *Opt. Express*, vol. 23, no. 15, pp. 19 596–19 604, Jul. 2015. DOI: `10.1364/OE.23.019596`. [Online]. Available: `https://opg.optica.org/oe/abstract.cfm?URI=oe-23-15-19596`.

[47] M. A. G. Porcel, F. Schepers, J. P. Epping, *et al.*, "Two-octave spanning supercontinuum generation in stoichiometric silicon nitride waveguides pumped at telecom wavelengths," *Opt. Express*, vol. 25, no. 2, pp. 1542–1554, Jan. 2017. DOI: `10.1364/OE.25.001542`. [Online]. Available: `https://opg.optica.org/oe/abstract.cfm?URI=oe-25-2-1542`.

[48] K. E. Zinoviev, A. B. González-Guerrero, C. Domínguez, and L. M. Lechuga, "Integrated bimodal waveguide interferometric biosensor for label-free analysis," *J. Lightwave Technol.*, vol. 29, no. 13, pp. 1926–1930, Jul. 2011. [Online]. Available: `https://opg.optica.org/jlt/abstract.cfm?URI=jlt-29-13-1926`.

[49] R. Diekmann, Ø. I. Helle, C. I. Øie, *et al.*, "Chip-based wide field-of-view nanoscopy," *Nature Photonics*, vol. 11, no. 5, pp. 322–328, May 2017, ISSN: 1749-4893. DOI: `10.1038/nphoton.2017.55`. [Online]. Available: `https://doi.org/10.1038/nphoton.2017.55`.

[50] A. Z. Subramanian, E. Ryckeboer, A. Dhakal, *et al.*, "Silicon and silicon nitride photonic circuits for spectroscopic sensing on-a-chip," *Photon. Res.*, vol. 3, no. 5, B47–B59, Oct. 2015. DOI: `10.1364/PRJ.3.000B47`. [Online]. Available: `https://opg.optica.org/prj/abstract.cfm?URI=prj-3-5-B47`.

[51] C. V. Poulton, M. J. Byrd, M. Raval, *et al.*, "Large-scale silicon nitride nanophotonic phased arrays at infrared and visible wavelengths," *Opt. Lett.*, vol. 42, no. 1, pp. 21–24, Jan. 2017. DOI: `10.1364/OL.42.000021`. [Online]. Available: `https://opg.optica.org/ol/abstract.cfm?URI=ol-42-1-21`.

[52] S. Gundavarapu, M. Belt, T. A. Huffman, *et al.*, "Interferometric optical gyroscope based on an integrated si3n4 low-loss waveguide coil," *Journal of Lightwave Technology*, vol. 36, no. 4, pp. 1185–1191, 2018. DOI: `10.1109/JLT.2017.2765918`.

[53] P. Muñoz, P. W. L. van Dijk, D. Geuzebroek, *et al.*, "Foundry developments toward silicon nitride photonics from visible to the mid-infrared," *IEEE Journal of Selected Topics in Quantum Electronics*, vol. 25, no. 5, pp. 1–13, 2019. DOI: `10.1109/JSTQE.2019.2902903`.

[54] *Home - LIGENTEC — ligentec.com*, `https://www.ligentec.com/`, [Accessed 17-08-2023].

[55] Aug. 2023. [Online]. Available: `https://www.lionix-international.com/`.

[56] *Silicon nitride photonic integration platform*, `http://www.imb-cnm.csic.es/index.php/en/clean-room/silicon-nitride-technology`, [Accessed 17-08-2023].

[57] K. Alexander, J. P. George, J. Verbist, *et al.*, "Nanophotonic pockels modulators on a silicon nitride platform," *Nature communications*, vol. 9, no. 1, pp. 1–6, 2018.

[58] C. T. Phare, Y.-H. Daniel Lee, J. Cardenas, and M. Lipson, "Graphene electro-optic modulator with 30 ghz bandwidth," *Nature photonics*, vol. 9, no. 8, pp. 511–514, 2015.

[59] D. Liang and J. E. Bowers, "Recent progress in lasers on silicon," *Nature photonics*, vol. 4, no. 8, pp. 511–517, 2010.

[60] Z. Zhou, B. Yin, and J. Michel, "On-chip light sources for silicon photonics," *Light: Science & Applications*, vol. 4, no. 11, e358–e358, 2015.

[61] H. Wada and T. Kamijoh, "Room-temperature cw operation of ingaasp lasers on si fabricated by wafer bonding," *IEEE Photonics Technology Letters*, vol. 8, no. 2, pp. 173–175, 1996.

[62] K. Mori, K. Tokutome, and S. Sugou, "Low-threshold pulsed operation of long-wavelength lasers on si fabricated by direct bonding," *Electronics Letters*, vol. 31, no. 4, pp. 284–285, 1995.

[63] H. Park, A. W. Fang, S. Kodama, and J. E. Bowers, "Hybrid silicon evanescent laser fabricated with a silicon waveguide and iii-v offset quantum wells," *Optics Express*, vol. 13, no. 23, pp. 9460–9464, 2005.

[64] E. Haglund, P. Westbergh, J. S. Gustavsson, *et al.*, "30 ghz bandwidth 850 nm vcsel with sub-100 fj/bit energy dissipation at 25–50 gbit/s," *Electronics Letters*, vol. 51, no. 14, pp. 1096–1098, 2015.

[65] E. Shim, A. Gil-Molina, O. Westreich, *et al.*, "Tunable single-mode chip-scale mid-infrared laser," *Communications Physics*, vol. 4, no. 1, p. 268, 2021.

[66] I. Vurgaftman, R. Weih, M. Kamp, *et al.*, "Interband cascade lasers," *Journal of Physics D: Applied Physics*, vol. 48, no. 12, p. 123 001, 2015.

[67] G. Boehm, M. Grau, O. Dier, *et al.*, "Growth of inas-containing quantum wells for inp-based vcsels emitting at 2.3 μm," *Journal of crystal growth*, vol. 301, pp. 941–944, 2007.

[68] S. Sprengel, G. K. Veerabathran, A. Andrejew, *et al.*, "Inp-based type-ii heterostructure lasers for wavelengths up to 2.7 um," in *Novel In-Plane Semiconductor Lasers XIV*, SPIE, vol. 9382, 2015, pp. 111–116.

[69] K. Vizbaras and M.-C. Amann, "Room-temperature 3.73 μm gasb-based type-i quantum-well lasers with quinternary barriers," *Semiconductor Science and Technology*, vol. 27, no. 3, p. 032 001, 2012.

[70] G. Belenky, L. Shterengas, G. Kipshidze, and T. Hosoda, "Type-i diode lasers for spectral region above 3 μm," *IEEE Journal of Selected Topics in Quantum Electronics*, vol. 17, no. 5, pp. 1426–1434, 2011.

[71] X. Li, J. X. B. Sia, W. Wang, *et al.*, "Phase noise reduction of a 2 μm passively mode-locked laser through hybrid iii-v/silicon integration," *Optica*, vol. 8, no. 6, pp. 855–860, 2021.

[72] S.-P. Ojanen, J. Viheriälä, N. Zia, *et al.*, "Widely tunable (2.47–2.64 µm) hybrid laser based on gasb/gainassb quantum-wells and a low-loss si3n4 photonic integrated circuit," *Laser & Photonics Reviews*, vol. 17, no. 7, p. 2 201 028, 2023. DOI: https://doi.org/10.1002/lpor.202201028. eprint: https://onlinelibrary.wiley.com/doi/pdf/10.1002/lpor.

202201028. [Online]. Available: https://onlinelibrary.wiley.com/doi/abs/10.1002/lpor.202201028.

[73] P. Karioja, T. Alajoki, M. Cherchi, *et al.*, "Multi-wavelength mid-IR light source for gas sensing," in *Society of Photo-Optical Instrumentation Engineers (SPIE) Conference Series*, Y. G. Soskind and C. Olson, Eds., ser. Society of Photo-Optical Instrumentation Engineers (SPIE) Conference Series, vol. 10110, Feb. 2017, 101100P, 101100P. DOI: 10.1117/12.2249126.

[74] Z. Nouman, "Wavelength-versatile gasb light emitters for hybrid photonics integrated circuits," Ph.D. dissertation, Tampere University, 2022.

[75] N. Zia, J. Viheriälä, E. Koivusalo, and M. Guina, "High-power single mode GaSb-based 2 m superluminescent diode with double-pass gain," *Applied Physics Letters*, vol. 115, no. 23, p. 231 106, Dec. 2019, ISSN: 0003-6951. DOI: 10.1063/1.5127407. eprint: https://pubs.aip.org/aip/apl/article-pdf/doi/10.1063/1.5127407/13314824/231106_1_online.pdf. [Online]. Available: https://doi.org/10.1063/1.5127407.

[76] M. Cherchi, S. Ylinen, M. Harjanne, M. Kapulainen, and T. Aalto, "Dramatic size reduction of waveguide bends on a micron-scale silicon photonic platform," *Opt. Express*, vol. 21, no. 15, pp. 17 814–17 823, Jul. 2013. DOI: 10.1364/OE.21.017814. [Online]. Available: https://opg.optica.org/oe/abstract.cfm?URI=oe-21-15-17814.

[77] W.-Q. Wei, A. He, B. Yang, *et al.*, "Monolithic integration of embedded iii-v lasers on soi," *Light: Science & Applications*, vol. 12, no. 1, p. 84, 2023.

[78] A. Y. Liu, R. W. Herrick, O. Ueda, P. M. Petroff, A. C. Gossard, and J. E. Bowers, "Reliability of inas/gaas quantum dot lasers epitaxially grown on silicon," *IEEE Journal of Selected Topics in Quantum Electronics*, vol. 21, no. 6, pp. 690–697, 2015.

[79] T. Komljenovic, M. Davenport, J. Hulme, *et al.*, "Heterogeneous silicon photonic integrated circuits," *Journal of Lightwave Technology*, vol. 34, no. 1, pp. 20–35, 2016. DOI: 10.1109/JLT.2015.2465382.

[80] A. De Groote, P. Cardile, A. Z. Subramanian, *et al.*, "Transfer-printing-based integration of single-mode waveguide-coupled iii-v-on-silicon broadband light emitters," *Optics Express*, vol. 24, no. 13, pp. 13 754–13 762, 2016.

[81] A. Spott, M. Davenport, J. Peters, *et al.*, "Heterogeneously integrated 2.0 μm cw hybrid silicon lasers at room temperature," *Optics letters*, vol. 40, no. 7, pp. 1480–1483, 2015.

[82] H. Lu, J. S. Lee, Y. Zhao, *et al.*, "Flip-chip integration of tilted vcsels onto a silicon photonic integrated circuit," *Opt. Express*, vol. 24, no. 15, pp. 16 258–16 266, Jul. 2016. DOI: `10.1364/OE.24.016258`. [Online]. Available: `https://opg.optica.org/oe/abstract.cfm?URI=oe-24-15-16258`.

[83] B. Song, C. Stagarescu, S. Ristic, A. Behfar, and J. Klamkin, "3d integrated hybrid silicon laser," *Opt. Express*, vol. 24, no. 10, pp. 10 435–10 444, May 2016. DOI: `10.1364/OE.24.010435`. [Online]. Available: `https://opg.optica.org/oe/abstract.cfm?URI=oe-24-10-10435`.

[84] S. Lin, X. Zheng, J. Yao, *et al.*, "Efficient, tunable flip-chip-integrated iii-v/si hybrid external-cavity laser array," *Opt. Express*, vol. 24, no. 19, pp. 21 454–21 462, Sep. 2016. DOI: `10.1364/OE.24.021454`. [Online]. Available: `https://opg.optica.org/oe/abstract.cfm?URI=oe-24-19-21454`.

[85] A. Moscoso-Mártir, J. Müller, J. Hauck, *et al.*, "Silicon photonics transmitter with soa and semiconductor mode-locked laser," *Scientific Reports*, vol. 7, no. 1, p. 13 857, 2017.

[86] N. Lindenmann, S. Dottermusch, M. L. Goedecke, *et al.*, "Connecting silicon photonic circuits to multicore fibers by photonic wire bonding," *Journal of lightwave Technology*, vol. 33, no. 4, pp. 755–760, 2014.

[87] M. J. Deen and P. K. Basu, *Silicon photonics: fundamentals and devices.* John Wiley & Sons, 2012.

[88] M. J. Deen and P. K. Basu, *Silicon Photonics Fundamentals and devices.* Wiley, 2012.

[89] Y. Gao, J.-C. Lo, S. Lee, *et al.*, "High-power, narrow-linewidth, miniaturized silicon photonic tunable laser with accurate frequency control," *Journal of Lightwave Technology*, vol. 38, no. 2, pp. 265–271, 2020. DOI: `10.1109/JLT.2019.2940589`.

[90] H. Guan, A. Novack, T. Galfsky, *et al.*, "Widely-tunable, narrow-linewidth iii-v/silicon hybrid external-cavity laser for coherent communication," *Opt. Express*, vol. 26, no. 7, pp. 7920–7933, Apr. 2018. DOI: `10.1364/OE.26.007920`. [Online]. Available: `https://opg.optica.org/oe/abstract.cfm?URI=oe-26-7-7920`.

[91] N. Kobayashi, K. Sato, M. Namiwaka, *et al.*, "Silicon photonic hybrid ring-filter external cavity wavelength tunable lasers," *Journal of Lightwave Technology*, vol. 33, no. 6, pp. 1241–1246, 2015. DOI: `10.1109/JLT.2014.2385106`.

[92] Y. Guo, X. Li, M. Jin, *et al.*, "Hybrid integrated external cavity laser with a 172-nm tuning range," *APL Photonics*, vol. 7, no. 6, p. 066 101, Jun. 2022, ISSN: 2378-0967. DOI: 10.1063/5.0088119. eprint: `https://pubs.aip.org/aip/app/article-pdf/doi/10.1063/5.0088119/16492717/066101\_1\_online.pdf`. [Online]. Available: `https://doi.org/10.1063/5.0088119`.

[93] J. Juvert, T. Cassese, S. Uvin, *et al.*, "Integration of etched facet, electrically pumped, c-band fabry-pérot lasers on a silicon photonic integrated circuit by transfer printing," *Opt. Express*, vol. 26, no. 17, pp. 21 443–21 454, Aug. 2018. DOI: 10.1364/OE.26.021443. [Online]. Available: `https://opg.optica.org/oe/abstract.cfm?URI=oe-26-17-21443`.

[94] A. Gallet, A. Shen, G. Levaufre, *et al.*, "Integrated hybrid iii-v/soi directly modulated dfb laser and ring resonator at 10 gbit/s," *IEEE Photonics Technology Letters*, vol. 29, no. 17, pp. 1424–1426, 2017. DOI: 10.1109/LPT.2017.2719123.

[95] D. Huang, M. A. Tran, J. Guo, *et al.*, "High-power sub-khz linewidth lasers fully integrated on silicon," *Optica*, vol. 6, no. 6, pp. 745–752, Jun. 2019. DOI: 10.1364/OPTICA.6.000745. [Online]. Available: `https://opg.optica.org/optica/abstract.cfm?URI=optica-6-6-745`.

[96] C. Xiang, W. Jin, J. Guo, *et al.*, "Narrow-linewidth iii-v/si/si3n4 laser using multilayer heterogeneous integration," *Optica*, vol. 7, no. 1, pp. 20–21, Jan. 2020. DOI: 10.1364/OPTICA.384026. [Online]. Available: `https://opg.optica.org/optica/abstract.cfm?URI=optica-7-1-20`.

[97] S. Dhoore, G. Roelkens, and G. Morthier, "Iii-v-on-silicon three-section dbr laser with over 12 nm continuous tuning range," *Opt. Lett.*, vol. 42, no. 6, pp. 1121–1124, Mar. 2017. DOI: 10.1364/OL.42.001121. [Online]. Available: `https://opg.optica.org/ol/abstract.cfm?URI=ol-42-6-1121`.

[98] G.-L. Su, M. N. Sakib, J. Heck, H. Rong, and M. C. Wu, "A heterogeneously-integrated iii-v/silicon interferometric widely tunable laser," in *OSA Advanced Photonics Congress (AP) 2019 (IPR, Networks, NOMA, SPPCom, PVLED)*, Optica Publishing Group, 2019, IW3A.1. DOI: 10.1364/IPRSN.2019.IW3A.1. [Online]. Available: `https://opg.optica.org/abstract.cfm?URI=IPRSN-2019-IW3A.1`.

[99] B. Stern, X. Ji, A. Dutt, and M. Lipson, "Compact narrow-linewidth integrated laser based on a low-loss silicon nitride ring resonator," *Optics letters*, vol. 42, no. 21, pp. 4541–4544, 2017.

[100] L. Chrostowski and M. Hochberg, *Silicon photonics design: from devices to systems*. Cambridge University Press, 2015.

[101] A. D. Simard, Y. Painchaud, and S. LaRochelle, "Integrated bragg gratings in spiral waveguides," *Opt. Express*, vol. 21, no. 7, pp. 8953–8963, Apr. 2013. DOI: `10.1364/OE.21.008953`. [Online]. Available: `https://opg.optica.org/oe/abstract.cfm?URI=oe-21-7-8953`.

[102] C. Xiang, W. Jin, J. Guo, *et al.*, "Narrow-linewidth iii-v/si/si3n4 laser using multilayer heterogeneous integration," *Optica*, vol. 7, no. 1, pp. 20–21, Jan. 2020. DOI: `10.1364/OPTICA.384026`. [Online]. Available: `https://opg.optica.org/optica/abstract.cfm?URI=optica-7-1-20`.

[103] R. Kitamura, L. Pilon, and M. Jonasz, "Optical constants of silica glass from extreme ultraviolet to far infrared at near room temperature," *Appl. Opt.*, vol. 46, no. 33, pp. 8118–8133, Nov. 2007. DOI: `10.1364/AO.46.008118`. [Online]. Available: `https://opg.optica.org/ao/abstract.cfm?URI=ao-46-33-8118`.

[104] *Ansys lumerical mode | optical waveguide & coupler design software lumerical.com*, `https://www.lumerical.com/products/mode/`, [Accessed 22-08-2023].

[105] [Online]. Available: `https://www.ansys.com/products/photonics/interconnect`.

[106] M. Ma, Z. Chen, H. Yun, *et al.*, "Apodized spiral bragg grating waveguides in silicon-on-insulator," *IEEE Photonics Technology Letters*, vol. 30, no. 1, pp. 111–114, 2017.

[107] S. Ojanen, N. Zia, J. Viheriälä, *et al.*, "Gasb/si3n4 narrow linewidth hybrid distributed bragg reflector lasers at 1.99 µm and 2.67 µm," *Manuscript awaiting publication*, 2023.

[108] D. Huang, M. A. Tran, J. Guo, *et al.*, "High-power sub-khz linewidth lasers fully integrated on silicon," *Optica*, vol. 6, no. 6, pp. 745–752, Jun. 2019. DOI: `10.1364/OPTICA.6.000745`. [Online]. Available: `https://opg.optica.org/optica/abstract.cfm?URI=optica-6-6-745`.